









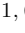













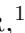







PHIBSS: Searching for Molecular Gas Outflows in Star-Forming Galaxies at $z = 0.5 - 2.6$

CAPUCINE BARFETY ¹ JEAN-BAPTISTE JOLLY ¹ NATASCHA M. FÖRSTER SCHREIBER ¹,
LINDA J. TACCONI ¹ REINHARD GENZEL ^{1,2} GIULIA TOZZI ¹ ANDREAS BURKERT ^{1,3}
JIANHANG CHEN ¹ FRANÇOISE COMBES ^{4,5} RIC DAVIES ¹ FRANK EISENHÄUER ^{1,6}
JUAN M. ESPEJO SALCEDO ¹ RODRIGO HERRERA-CAMUS ⁷ LILIAN L. LEE ¹
MINJU M. LEE ^{8,9} DAIZHONG LIU ^{1,10} DIETER LUTZ ¹ THORSTEN NAAB ¹¹
ROBERTO NERI ¹² AMIT NESTOR SHACHAR ¹³ STAVROS PASTRAS ^{1,11} CLAUDIA PULSONI ¹,
SEDONA H. PRICE ¹⁴ ALVIO RENZINI ¹⁵ KARL SCHUSTER ¹² TARO T. SHIMIZU ¹
AMIEL STERNBERG ¹³ ECKHARD STURM ¹ HANNAH ÜBLER ¹ AND STIJN WUYTS ¹⁶

¹Max-Planck-Institut für extraterrestrische Physik, Giessenbachstrasse, D-85748 Garching, Germany

²Departments of Physics and Astronomy, University of California, Berkeley, CA 94720, USA

³University Observatory Munich (USM) Scheinerstrasse 1, D-81679 Munich, Germany

⁴Observatoire de Paris, LUX, CNRS, PSL Univ., Sorbonne University, Paris, France

⁵Collège de France, 11 Pl. Marcelin Berthelot, 75231 Paris, France

⁶Department of Physics, Technical University of Munich, 85748 Garching, Germany

⁷Departamento de Astronomía, Universidad de Concepción, Barrio Universitario, Concepción, Chile

⁸Cosmic Dawn Center (DAWN), Denmark

⁹DTU-Space, Technical University of Denmark, Elektrovej 327, DK2800 Kgs. Lyngby, Denmark

¹⁰Purple Mountain Observatory, Chinese Academy of Sciences, 10 Yuanhua Road, Nanjing 210023, People's Republic of China

¹¹Max-Planck Institute for Astrophysics, Karl Schwarzschildstrasse 1, 85748, Garching, Germany

¹²Institut de Radioastronomie Millimétrique (IRAM), 300 Rue de la Piscine, 38400 Saint-Martin-d'Hères, France

¹³School of Physics and Astronomy, Tel Aviv University, Tel Aviv 69978, Israel

¹⁴Department of Physics and Astronomy and PITT PACC, University of Pittsburgh, Pittsburgh, PA 15260, USA

¹⁵Osservatorio Astronomico di Padova, Vicolo dell'Osservatorio 5, Padova, I-35122, Italy

¹⁶Department of Physics, University of Bath, Claverton Down, Bath, BA2 7AY, UK

ABSTRACT

We present an analysis of millimeter CO observations to search and quantify signatures of molecular gas outflows. We exploit the large sample of $0.5 < z < 2.6$ galaxies observed as part of the PHIBSS1/2 surveys with the IRAM Plateau de Bure interferometer, focusing on the 154 typical massive star-forming galaxies with CO detections (mainly CO(3-2), but including also CO(2-1) and CO(6-5)) at signal-to-noise (SNR) > 1.5 and available properties (stellar mass, star formation rate, size) from ancillary data. None of the individual spectra exhibit a compelling signature of CO outflow emission even at high SNR > 7 . To search for fainter outflow signatures, we carry out an analysis of stacked spectra, including the full sample, as well as subsets, split in terms of stellar mass, redshift, inclination, offset in star formation rate (SFR) from the main sequence, and AGN activity. None of the physically motivated subsamples show any outflow signature. We report a tentative detection in a subset statistically designed to maximize outflow signatures. We derive upper limits on molecular gas outflow rate and

mass loading factors η based on our results and find $\eta \leq 2.2 - 35.4$, depending on the subsample. Much deeper CO data and observations of alternative tracers are needed to decisively constrain the importance of cold molecular gas component of outflows relative to other gas phases.

Keywords: Submillimeter – Galaxies, Galaxies – Feedback, Galaxies – high redshift, ISM – jets and outflows

1. INTRODUCTION

Feedback in the form of outflows has long been invoked to explain observed galaxy scaling relations and stages of galaxy evolution. They are believed to be a key part of the baryon cycle, mixing and redistributing gas within and around galaxies (Tumlinson et al. 2017; Péroux & Howk 2020). As such, they are important mechanisms to shape the mass-metallicity relation, set metallicity gradients within galaxies (Davé et al. 2011; Sanders et al. 2018), and explain the large reservoirs of baryons and metals in the intergalactic medium (IGM) (Peeples et al. 2014; Tumlinson et al. 2017). They are also invoked to reconcile theoretical and numerical predictions with observations, such as the galaxy mass function (e.g., Schaye et al. 2015), the color bi-modality (blue, young star-forming galaxies (SFGs) vs. red passive galaxies), or even scaling relations between black hole mass and host galaxy bulge properties (Dekel & Silk 1986; Mutch et al. 2013).

Outflows originate from two processes: stellar winds and supernovae in star-forming regions (Murray et al. 2005; Hopkins et al. 2014) and active galactic nuclei (AGN) accretion (Fabian 2012; King & Pounds 2015). Depending on their driving mechanism, the outflow properties can vary strongly. Star formation (SF)-driven outflows have velocities $\sim 10^2$ km/s, unlikely to escape the potential well of the galaxy (e.g., Shapley et al. 2003; Newman et al. 2012a; Leroy et al. 2015; Förster Schreiber et al. 2019; Davies et al. 2019; Avery et al. 2021), regulating SF and galaxy growth over the span of

galaxies’ life on and above the main sequence (MS; Reichardt Chu et al. 2025). On the other hand, AGN-driven outflows happen over shorter timescales and are typically more powerful, driving faster winds ($\gtrsim 10^3$ km/s) reaching further into the circumgalactic medium (Davies et al. 2020; Herrera-Camus et al. 2019; see Harrison & Ramos Almeida 2024 for a recent review). Defining the mass loading factor $\eta = \frac{M_{\text{out}}}{\text{SFR}}$ as a measure of the dominant gas depletion mechanism, where $\eta > 1$ is interpreted as outflows carrying enough mass to deplete the gas faster than SF can, AGN-driven outflows typically have higher mass loading factors than SF-driven outflows, and thus affect SF more efficiently (Fiore et al. 2017).

At $z = 1 - 3$, the cosmic star formation rate (SFR) and AGN density reach their peak, and so does the cold molecular gas fraction in galaxies (Madau & Dickinson 2014; Tacconi et al. 2020). During this “cosmic noon” epoch, roughly half of the present-day stellar mass is formed, most of which ($\sim 90\%$) is taking place in SFGs on/near the MS (Rodighiero et al. 2011; Speagle et al. 2014; Whitaker et al. 2014). Studying outflows in MS SFGs at $z \sim 1 - 3$ is important to quantify the impact of SF and AGN feedback on the growth and evolution of the galaxy population as a whole. Observational studies have reported that galactic scale outflows are ubiquitous at this epoch (see Förster Schreiber & Wuyts 2020 and Veilleux et al. 2020 for recent reviews). At these redshifts, most outflow studies are in the ionized gas phase, detected both through rest-UV inter-

stellar features (e.g., Shapley et al. 2003; Talia et al. 2012, 2017; Weldon et al. 2022; Calabrò et al. 2022; Kehoe et al. 2024) and through optical emission lines such as $H\alpha$, $H\beta$, [OIII] and [NII] (e.g., Genzel et al. 2011, 2014; Harrison et al. 2016; Leung et al. 2017, 2019; Swinbank et al. 2019; Förster Schreiber et al. 2019; Davies et al. 2020; Concas et al. 2022; Weldon et al. 2024; Kehoe et al. 2024). This body of work highlighted correlations of outflow incidence with stellar mass, star formation rate (SFR), distance from the MS (Δ MS), and redshift. However, looking into the mass loading factor η , studies find typical values of $\eta < 1$ for both AGN- and SF-driven ionized gas outflows (e.g., Freeman et al. 2019; Förster Schreiber et al. 2019; Davies et al. 2020). These low values of η for ionized gas outflows are in contradiction with the scenario where outflows are believed to regulate SF on galactic scales.

These results at cosmic noon are unsurprising as the ionized gas phase may not carry the bulk of the mass (although they carry substantial energy and momentum; e.g., Förster Schreiber et al. 2019). At all redshifts, observations show that outflows are complex and multi-phase, with observations across the whole wavelength range spanning wide physical scales (Genzel et al. 2011, 2014; Bolatto et al. 2013b; Fluetsch et al. 2019; Herrera-Camus et al. 2020a; Levy et al. 2021; Reichardt Chu et al. 2022; Tozzi et al. 2021; Kehoe et al. 2024; Davies et al. 2024b; Parlanti et al. 2024), a result corroborated by simulations (Cooper et al. 2008; Costa et al. 2015; Schneider et al. 2018; Ward et al. 2024). Observations of the cold molecular phase of outflows in local galaxies, through CO transition lines or P-Cygni profiles in far-infrared (IR) OH lines, find that they are much more efficient drivers of material than their ionized gas counterparts (Sturm et al. 2011; Veilleux et al. 2013; Bolatto et al. 2013a; Contursi et al. 2013; Davies et al. 2014; González-Alfonso et al.

2017; Krieger et al. 2019; Schneider et al. 2020; Vijayan et al. 2024). Except for one AGN-hosting MS galaxy at $z > 2$ (Herrera-Camus et al. 2019), detections of molecular gas outflows at cosmic noon have been exclusively in luminous AGNs and quasars (e.g., Brusa et al. 2018; Chartas et al. 2020; Davies et al. 2020), which may not be representative of the general population of galaxies. Another stacking analysis of CO observations of cosmic noon MS and starbursting galaxies find no statistically significant outflow detection (Langan et al. in prep). This is partly due to the challenging nature of CO observations at higher redshift; however, in this framework, their incidence and properties among cosmic noon galaxies and their impact on galaxy evolution have yet to be established.

This paper aims to address this outstanding issue by exploiting the PHIBSS 1/2 datasets of mostly main-sequence $z = 0.5 - 2.6$ SFGs to search for molecular gas outflow signatures in CO mid- J transitions. The sample is unbiased towards AGN activity and offers a population-averaged view of typical SFGs at cosmic noon, and is the largest, most complete sample available to conduct this analysis at cosmic noon. In Section 2, we introduce the survey and galaxy sample used in the analysis, as well as the details of the observations. In Sections 3 and 4, we present the details of the analysis and results of individual and stacked galaxy spectra. We present the tests of the method in Section 5. We discuss the implications of our results in Section 6, and summarize our conclusions in Section 7. Throughout the paper we use a standard Λ CDM cosmology with $H_0 = 70 \text{ km s}^{-1} \text{ Mpc}^{-1}$, $\Omega_m = 0.3$, and $\Omega_\Lambda = 0.7$.

2. OBSERVATIONS

2.1. *The PHIBSS sample*

The Plateau de Bure High- z Blue Sequence Survey (PHIBSS) is a molecular gas survey of 174 typical MS galaxies spanning $0.5 \leq z \leq 2.6$.

Observations were carried out in two large programs, PHIBSS1 (2009-2011; PIs: L. Tacconi & F. Combes) and PHIBSS2 (2013-2017; PIs: F. Combes, S. García-Burillo, R. Neri & L. Tacconi), using the Plateau de Bure Interferometer (PdBI)/NOEMA. Observations cover a range of beam sizes from $0.65 - 9.4'' \times 0.65 - 5.25''$, with spectral resolutions from 7 km/s to 88 km/s. Detailed descriptions of the observations and sample can be found in Tacconi et al. (2013, 2018) and Freundlich et al. (2019).

The observations cover the CO(3-2) line for 99 galaxies at redshift $1.00 \leq z \leq 2.55$, the CO(2-1) line for 70 lower redshift ($0.50 \leq z \leq 1.53$) galaxies, and the CO(6-5) line for the remaining 5 galaxies ($2.01 \leq z \leq 2.33$). For each galaxy, we compute the integrated SNR of the narrow emission line and discard detections below $\text{SNR} = 1.5$. Although this threshold is lower than what is typically considered significant, the stacking process aims to uncover the signal hidden within the noise, so we retain these detections in the stack. This process brings the sample down to 154 galaxies, with median $\langle z \rangle = 1.04$, $\langle \log(M_*/M_\odot) \rangle = 10.8$, $\langle R_e \rangle = 4.4$ kpc and $\langle \Delta\text{MS} \rangle = 0.14$ dex (see Table 1, and the corresponding property distributions are plotted in Appendix A, Fig. 9). The individual galaxy properties are reported in Table 2, in Appendix A. The distribution is plotted in Fig. 1 as a function of their distance from the MS (computed following the parametrization from Whitaker et al. 2014), stellar mass, and redshift. In addition, we verified that the SNR cut does not change our results or improve the SNR of the stacked spectra by repeating the cut with higher threshold values ($\text{SNR} > 3$ and > 5).

2.2. AGN Identification

Since AGNs can be the main driver of strong outflows in the stellar mass range covered by PHIBSS (e.g., Förster Schreiber et al. 2019; Davies et al. 2024b), we identify the AGNs among the sample using publicly available

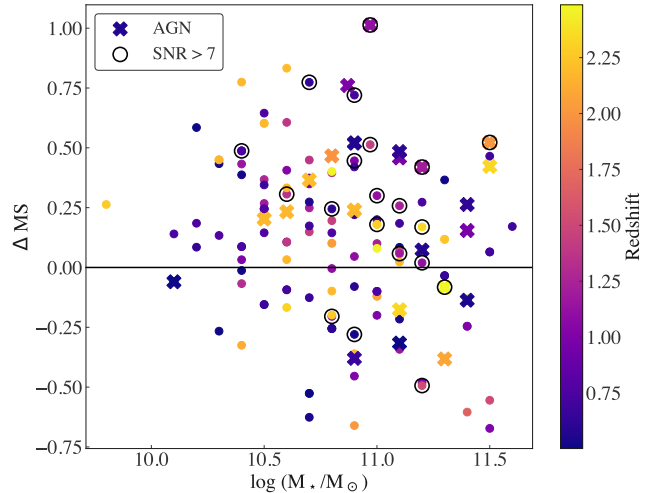


Figure 1. Distribution of the PHIBSS sample used in this paper in distance from the Main Sequence (MS) following the parametrization from Whitaker et al. (2014), as a function of stellar mass. Circled in solid black are the galaxies detected with $\text{SNR} > 7$, and galaxies marked with a cross are flagged as AGN-hosting.

multi-wavelength catalogs. We classify the galaxies as AGN based on X-ray, mid-IR, optical, and radio flux diagnostics.

First, we cross-correlate the PHIBSS catalogs with the *Chandra* X-ray source catalog¹. We then apply a luminosity cut based on the galaxies' expected 2 – 10 keV X-ray luminosity from their SFR (Symeonidis et al. 2014), such that galaxies with an associated X-ray detection 1 dex higher than the expected luminosity purely from star formation are flagged as AGNs. From the full sample, 136 galaxies are in *Chandra* coverage, 24 of which have an associated X-ray detection. Of these 24, 17 fulfill the aforementioned criteria. Next, we cross-match the PHIBSS survey with the MOSDEF public line-emission catalogs (Kriek et al. 2015; Reddy et al. 2015; Shapley et al. 2015), finding 15 galaxies in both samples. We investigate the $[\text{OIII}]\lambda 5007/\text{H}\beta$ vs $[\text{NII}]\lambda 6584/\text{H}\alpha$ BPT diagram (Baldwin et al. 1981), using the

¹ <https://cxc.harvard.edu/csc/index.html>

upper limit star-forming abundance sequence reported by Kewley et al. (2013) at the average redshift $\bar{z} = 2.15$ of the 15 galaxies. We find 6 galaxies lying above the limit, which are thus classified as AGN. Following this, we use the *Spitzer*/IRAC photometry available for 116 of the galaxies to identify AGN based on the color criteria presented by Donley et al. (2012). Eight of the galaxies are classified as AGN based on their mid-IR colors. Lastly, we cross-match the sample with public source catalogs from JVLA radio surveys. Following Delvecchio et al. (2017), we identify as AGNs sources with $L_{1.4\text{GHz}}$ exceeding the value expected from the far-IR-radio scaling relation for star-forming galaxies. Seven of the PHIBSS galaxies satisfy this criterion. In total, 24 galaxies fulfill one or more of the above criteria. The galaxies are reported as AGN in Table 2. We note that due to the sample selection aiming for typical star-forming galaxies, none of the sources in our sample are luminous AGNs or have emission dominated by AGN contribution.

3. METHODS

Our analysis ultimately uses spectral stacking to uncover outflow signatures in the line profile. The stacking process applied in this analysis consists of averaging spectra with potential underlying outflow emission, with various widths, amplitude, and central velocities. In these conditions, we expect outflow signatures in the stacked spectra to appear as a secondary faint broad component centered close to a brighter, narrower emission line originating from gravitationally bound material in the galaxies. This section describes the procedure we apply to retrieve such outflow signatures adequately.

3.1. Spectrum Extraction

We use the following method to extract the spectra of individual galaxies and maximize the SNR. First, we define a beam-sized aperture at

the center of the data cube, sum the spectra of each pixel within the aperture, and perform a Gaussian fit to the line profile. Using the fit results, we collapse the initial data cubes along the velocity channels, summing all the velocity bins within the FWHM of the line and centering on the best-fit velocity. We then run SExtractor (Bertin & Arnouts 1996) on the collapsed image to determine the area of detection of the galaxy and create a spatial mask of this detection. Since, in most cases, the detected area by SExtractor is smaller than the beam size, we use the beam size as the aperture for the mask, which we center on the SExtractor coordinates. When the detected area is larger than the beam, we use this as the aperture for the mask. Finally, we sum all non-masked pixels in the 3D cube and fit the resulting spectrum with a single Gaussian. We iterate over this process three times to obtain the best possible mask (i.e.: the mask for which the integrated spectrum returns the line with the highest SNR). Iterating over this process optimizes the detection area and the estimates of the central velocity and FWHM, which are both crucial to our stacking analysis for precise alignment and to correctly re-bin the spectra (see Sec. 3.2). The final apertures have median major axis $\langle a \rangle = 25_{-10}^{+14}$ kpc and minor axis $\langle b \rangle = 19_{-6}^{+11}$ kpc. The final FWHMs are reported in Table 2, and their distribution is shown in Appendix A, Fig. 9.

After the final iteration, we extract the spectra from the masked cube. We also scale each spectrum's flux by normalizing it to the best-fit amplitude of the Gaussian fit to the emission line, such that the brightest galaxies do not dominate the stacked spectrum, as we are interested in the population average.

3.2. Spectral Re-binning

The spectral stacking of emission lines with different widths, due to the different ranges of projected velocities for different galaxies, can lead to the creation of a broad-like component

in the stacked line profile, which can be misinterpreted as an outflow signature in the stacked profile (see, e.g. Sec. 5.2; Stanley et al. 2019 and Concas et al. 2022 for detailed discussions).

To mitigate this shortcoming of the stacking method, we re-bin the spectral channels of each galaxy spectrum according to their estimated FWHM such that each line would have a FWHM covering the same number of spectral channels. Upon inspection of the distribution of FWHMs in our sample (see Appendix A, Fig. 9), we choose a width of 7 channels as the common line width for re-binning, to favor down-sampling but to limit the bin size change to a moderate amount (with a maximum factor of 6)². After re-binning, the average channel width is 37 ± 25 km/s. This method impacts the accuracy of the velocity information one can retrieve from the spectra but preserves the line shapes such that any underlying broad component revealed by the stacking could not be attributed to numerical effects. We investigate in Sec. 5 whether re-binning impacts our ability to retrieve real underlying outflows.

3.3. Spectral Stacking

After re-binning, we stack the normalized spectra of the individual galaxies using the `LINESTACKER` package presented in Jolly et al. 2020. Given a central velocity for each spectrum (here we use the best-fit velocity retrieved in the spectrum extraction process; see Sec. 3.1), the code aligns the spectra and computes the mean of the flux in each spectral channel, where each spectrum is given the same weight in the mean. We stack both the full sample and the following sub-samples (median properties are listed in Table 1): above and below $\log(M_*/M_\odot) = 10.7$, above and below $\Delta MS = 0.2$, and above and below $z = 1.7$. These choices are motivated

by the trends in ionized gas outflow incidence of Förster Schreiber et al. 2019, corresponding to the stellar mass (ΔMS) above which AGN (SF)-driven outflows become more frequent. We also separately stack the sub-sample of 24 AGN-hosting galaxies selected in Sec. 2.2. Finally, since outflow detection is also dependent on galaxy orientation, we create and stack subsamples divided by inclination for the 117 galaxies for which we have the inclination: below 30° , between 30° and 60° , and above 60° . The stacking results for the full sample, the AGN sample, and the sub-samples are presented and discussed in Sec. 4.2.

To estimate the noise level in the stacked spectra, we extract a “blank” spectrum from an empty sky region using the same aperture as used to extract the corresponding galaxy spectrum. After stacking them following the same procedure described above, we take the resulting standard deviation as the noise estimate for each stack. Using this method instead of the noise directly in the spectra allows us to ensure we do not include any “hidden” signal in the noise estimation.

Finally, we repeat the stacking procedure on the same sample and sub-samples but weigh each spectrum by its noise, such that noisier spectra weigh less in the stack. There are no differences in the results from both stacking prescriptions, and for the rest of the analysis, we use the results from the non-weighted stack.

4. RESULTS

4.1. Inspection of Individual Spectra

As a first step of the analysis, we examine the individual spectra with integrated $SNR > 7$ to search for the presence of outflow signatures in these deeper data sets, as this SNR value indicates robust emission line detection. Out of the full sample of 154 galaxies, 20 have emission lines with SNR above this value ($SNR = 7.3 - 20.8$, black circles in Fig. 1), four of

² We have also repeated the measurements using 9, the median of the FWHM distribution, as the reference value, and observed that it does not affect the results

which are identified as AGNs (all galaxies have coverage by either *Chandra*, MOSDEF, *Spitzer* or VLA, see Sec. 2.2). This subsample of high SNR spectra has median $\langle \Delta MS \rangle = 0.28$, $\langle z \rangle = 1.16$ and $\langle \log(M_*/M_\odot) \rangle = 10.99$ (see Table 2 and Fig 1), thus preferentially probing higher stellar masses (85% have $\log(M_*/M_\odot) > 10.7$), and slightly higher z and ΔMS .

Three of these galaxies exhibit notable asymmetry in their CO line profile. For two of them, the line profile is explained by the fact that the galaxy is well detected over more than one beam and that the mask applied in Sec. 3.1 does not cover the full galaxy. In this case, the line from the initial mask has an asymmetric shape and becomes the double-peaked profile expected from the galactic rotation after adjusting the mask (see Appendix B, Fig. 10).

For the remaining spectrum, from a galaxy associated with an AGN, it is difficult to ascertain whether the spectrum shows signs of molecular gas outflows, as the line profile displays signs of asymmetry similar to what is described above (see Appendix B, Fig. 11). Still, the issue does not appear to come from the masking. Through visual inspection of the cube and based on the strength of the asymmetric feature, we favor the fact that the profile is indeed due to galaxy rotation and is not an outflow signature.

Thus, we observe that prominent outflow signatures are not prevalent at high SNR, even for a subsample with galaxy properties for which we would expect higher outflow incidences and strength (high mass, high redshift, high SFR, AGN hosting). We also investigate later the presence of extended emission beyond the initial masking process (see Sec. 4.3). Moreover, we do not expect the masking issue presented above to affect our results more broadly as, in most cases, the detected area is smaller than the beam size, so the majority of our masks encompass more than the detection.

To fully exploit the PHIBSS data set, we now use the stacked spectra to search for potential outflow signatures that cannot be identified on an individual galaxy basis.

4.2. Outflow Retrieval from Stacks

The results from the stacking of the spectra are shown in Fig. 2 for the full sample and in Figs. 3 & 4 for subsamples defined in Sec. 3.3. The stacked lines are fit both with a single and double Gaussian component, where the fit has the following constraints: (1) one component cannot have both the larger amplitude and the larger width, (2) the amplitude of both components should be positive, (3) the center of the second component should be within 10 channels of the center of the first component, to avoid fitting noise peaks on the edges of the spectrum. In addition, for each channel, we define as the error on the flux the error derived in Sec. 3.3 from the stacked “blank” spectra, scaled by the number of sources stacked in that particular channel ($\sigma_{\text{noise}} \propto 1/\sqrt{N_{\text{obj}}}$ where N_{obj} is the number of sources stacked). This number varies from channel to channel as all spectra do not cover the same spectral range. In all cases, the single Gaussian fit residuals, normalized by the noise in the spectra, are displayed below the stacked spectrum in Figs. 2, 3 & 4. Since some of the individual integrated galaxy spectra display the double-peaked profile expected from inclined rotating disks, this feature sometimes propagates in the stacked spectra and can be seen in the residuals. However, no clear outflow signature is visible.

For completeness, we perform a two-Gaussian fit to the spectra and observe that it does not improve the goodness-of-fit. Indeed, the reduced χ^2 of the single Gaussian fit is systematically lower than that of the double Gaussian fit. We also perform an analysis of the Bayesian in-

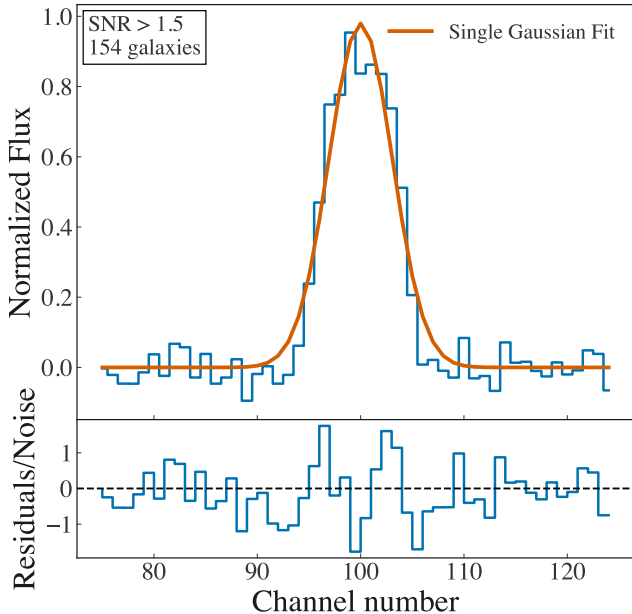


Figure 2. *Upper Panel:* Stacked spectrum (light blue curve) of the full sample of 154 galaxies. Overlaid on the spectrum is the best-fit single Gaussian profile (solid orange). Fitting shows that no significant outflow component is detected in the stacked spectrum. *Bottom Panel:* Normalized fit residuals ($\frac{\text{data}-\text{model}}{\text{noise}}$) from the single Gaussian fitting.

formation criterion (BIC, Schwarz 1978)³ of our single and double Gaussian fits. To do so, we define $\Delta\text{BIC} = \text{BIC}_{\text{sing}} - \text{BIC}_{\text{doub}}$ as the difference between the BIC of the single Gaussian fit and the double Gaussian fit, respectively, where $\Delta\text{BIC} > 0$ favors the double Gaussian model to fit the data, and $\Delta\text{BIC} > 10$ is strong evidence that a double Gaussian fit is needed to fit the data (Liddle 2007). For all stacked spectra, $\Delta\text{BIC} < 0$, in line with the result that there are no outflow signatures in the stacks. In addition, the flux of the very low amplitude broad component is systematically below the noise level (see Fig. 6, as determined following the procedure outlined in Sect. 4.5). Therefore, there is no statistically significant evidence for

³ The BIC is defined as $\text{BIC} = k \ln(n) + \chi^2$, where k is the number of free parameters, and n is the number of fitted data points (Hogg et al. 2010).

a broad component associated with outflows in the stacked spectra.

4.3. Investigating the Extended Emission

Since outflows in various phases have been observed in extended regions in the outskirts of their host galaxies (e.g., Genzel et al. 2011, 2014; Fabian 2012; Newman et al. 2012b,a; Förster Schreiber et al. 2014, 2019; Leroy et al. 2015; Herrera-Camus et al. 2019; Davies et al. 2020), we also looked into the extended emission around our sample. To do so, we investigate the spectra extracted from both larger apertures and annuli apertures centered on the galaxies. The larger apertures are designed by “dilating” the original mask by 10kpc in every direction, while the “annuli” apertures are the difference between the bigger and original apertures. The 10kpc increase in size is chosen based on the extent of the molecular gas outflow in Herrera-Camus et al. (2019). Finally, we perform the same stacking analysis and fitting as previously on these newly extracted spectra. While both methods do reveal spatially extended emission that is undetected in individual cubes and thus missed by the nominal masks employed, fitting the double Gaussian profile to the lines returns the same result as for the initial aperture: we observe no faint broad component in the stacked profile, and the fit residuals show no improvement from performing a two-component Gaussian fit (see Appendix C for the stacked profiles from the extended and annuli apertures respectively).

4.4. Subset-sampling Analysis

We created the sub-samples described in Sec. 3.3 based on observed correlations between ionized gas outflow incidence and galaxy properties. However, if molecular gas outflows have different correlations or are less prevalent in galaxies, a non-matched choice of parameter space leaves too much “dilution” from sources with weak or absent outflow signatures. We

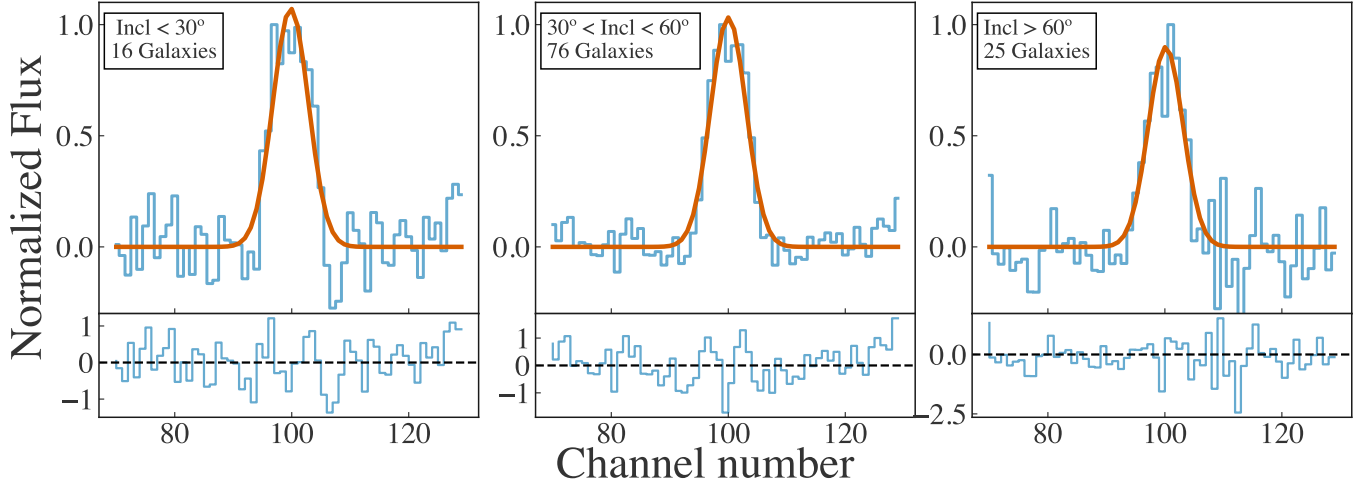


Figure 3. *Upper Panel:* Stacked spectra (light blue curves) for the three bins in inclination. Similar to Fig. 2, we plot the best-fit single Gaussian model to the profiles (solid orange) and the fit residuals normalized by the error below each plot. As in Fig. 2, there is no broad component signature, i.e., no outflow detection in any of the stacks.

apply the subset-sampling analysis described in Stanley et al. (2019) to search for potential outflows in sub-samples that may not match the subsets defined by M_* , ΔMS , or AGN as defined in Sect. 3.3 based on ionized gas outflow studies.

Following the methodology, we design a subset of spectra by randomly selecting between 3 and 154 galaxies from the full sample. These are then stacked and fitted with our two-component Gaussian model. Each spectrum in the subset is assigned a grade based on the strength of the broad Gaussian fit component (i.e. how much flux is contained in the secondary broad component, where the flux is defined as $F_{\text{output}} = \sqrt{2\pi} \times A_{\text{out}} \times \sigma_{\text{out}}$, with A_{out} the best fit broad component amplitude and σ_{out} is the best fit broad component width). The process is repeated 100,000 times, each time randomly selecting spectra from the full sample, such that every spectrum is graded. This allows us to select a final sub-sample of galaxies with the highest grade, i.e., the best candidates to have an outflow. We then repeat the stacking process on the galaxies with the highest grades and evalu-

ate if we retrieve any underlying broad component.

Using this method, we find a subset of 41 galaxies (26% of the full sample, marked with a † symbol in Table 2) for which the stacked spectrum displays a tentative outflow signature, evaluated at 4σ , shown in Fig. 5. The residuals of the best-fit show improvement when using a double Gaussian model, and its reduced χ^2 is closer to one than that of the single Gaussian fit. Repeating the analysis of the BIC presented in Sec. 4.2, we find $\Delta\text{BIC} = 6$, which favors the double Gaussian fit as better for the spectrum. All but one galaxy have coverage by either *Chandra*, *MOSDEF*, *Spitzer* or *VLA*, and 13 are flagged as AGN (Sec. 2.2). We investigate the subsample properties in Appendix D and find no striking correlation between the tentative outflow detection and the galaxies’ physical properties, except for a slight bias towards higher masses ($\langle \log(M_*/M_\odot) \rangle = 10.95$). This might be consistent with the trend in M_* reported by, e.g., Förster Schreiber et al. 2019 in the case of predominant AGN-driven winds. We also investigate the outflow properties (outflow mass, mass outflow rate, mass

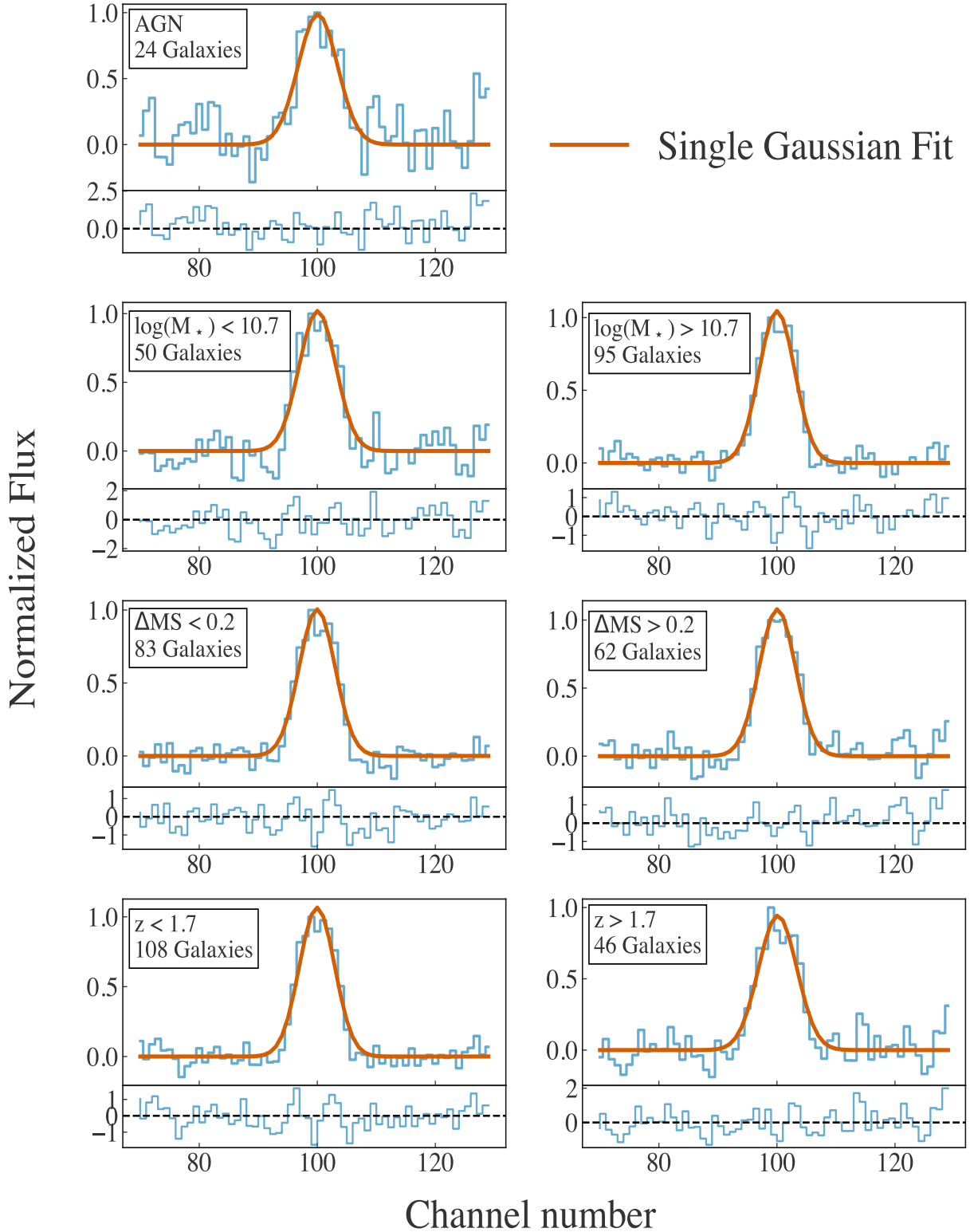


Figure 4. Stacked spectra (blue curves) for all the 7 subsamples described in Sec. 3.3. Overlaid on the spectrum is the best-fit single Gaussian profile (solid orange). Fitting shows that no significant outflow component is detected in the stacked spectrum. *Bottom Panel:* Similar to Figs 2 and 3, normalized fit residuals ($\frac{\text{data}-\text{model}}{\text{noise}}$) from the single Gaussian fitting.

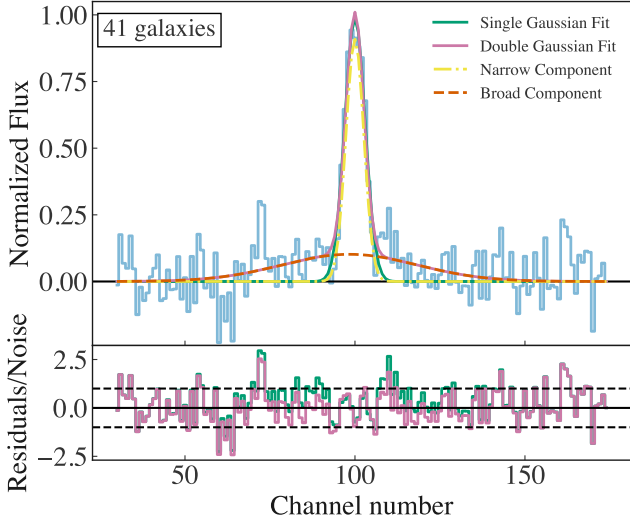


Figure 5. Stacked spectrum of the 41 galaxies with the highest grade in the subset sampling analysis, along with the best-fit single Gaussian (solid Green), double Gaussian (solid purple). The two individual components of the double Gaussian fit are also plotted (dot and dashed yellow for the narrow component and dashed orange for the broad component). The bottom panel shows both models’ best-fit residuals (normalized by the noise). The black dashed lines indicate where $\frac{\text{data}-\text{model}}{\text{noise}} = 1$.

loading factor) from the detection in Sec. 4.5 and report the values in Table 1. Still, the low significance of the result and lack of outflow signature in the stacks of high-mass and AGN-hosting galaxies prevent any firm conclusion with the data in hand. In addition, a caveat of the subsampling analysis is that it can result in selecting the galaxies whose noise properties will stack positively, mimicking an outflow detection. We try varying the re-binning of the spectra and stacking the spectra extracted from the extended apertures of the galaxies and observe that the feature remains.

4.5. Upper Flux Limit

From our non-detections, we measure an upper limit on the flux an outflow could have based on the noise level measured in the empty stacked spectrum. Defining a detection above the noise level as $3\sigma_{\text{noise}}$, where σ_{noise} is the standard de-

viation per channel of our empty spectrum (see Sec. 3.3), we compute the upper flux limit of a putative broad component using:

$$F_{UL} = 3\sigma_{\text{noise}}\sqrt{N_{\text{ch}}}$$

where $N_{\text{ch}} = 2 \times 3 \times \sigma_{\text{out, ch}}$ is the number of channels spanned by this hypothetical Gaussian, defined as 3 standard deviations $\sigma_{\text{out, ch}}$ (in channels) on both sides of the Gaussian center to encompass $> 99\%$ of the flux⁴. As we do not have a value of σ_{out} , we compute this upper limit for values of σ_{out} between $0.07 - 10 \times$ the narrow component width $\sigma_{\nu, \text{systemic}}$ (see Fig. 6).

To investigate what this limit represents for the outflow and what parameter space this hypothetical outflow might span, we create a grid of 500 flux values for a set of broad-to-narrow amplitude ratio ($0.01 - 0.8$) and broad-to-narrow linewidth ($0.07 - 10$; which is also translated to physical values using the average channel width and average line amplitude of the stacked spectra). We plot this grid as the background of Fig. 6, as function of the input parameters. We note that for outflow width below $2 \times$ the galaxy line width, it will be almost impossible to separate the galaxy emission from the outflow emission, if the lines have the same central velocity (see also Sec. 5, Fig. 7). On the other hand, if the outflow central velocity is shifted with respect to the galaxy emission line’s, it should be possible to detect an outflow with a small width.

This upper flux limit is computed by assuming the maximum possible flux value a stacked outflow component might have under the noise level. If all the galaxies in our sample have an outflow participating in the average - i.e. if the outflow incidence is 100% -, the flux limit computed above corresponds to the grey shaded

⁴ This is a conservative approach; if considering the flux within the FWHM, the upper limits would be lower by a factor of 1.6

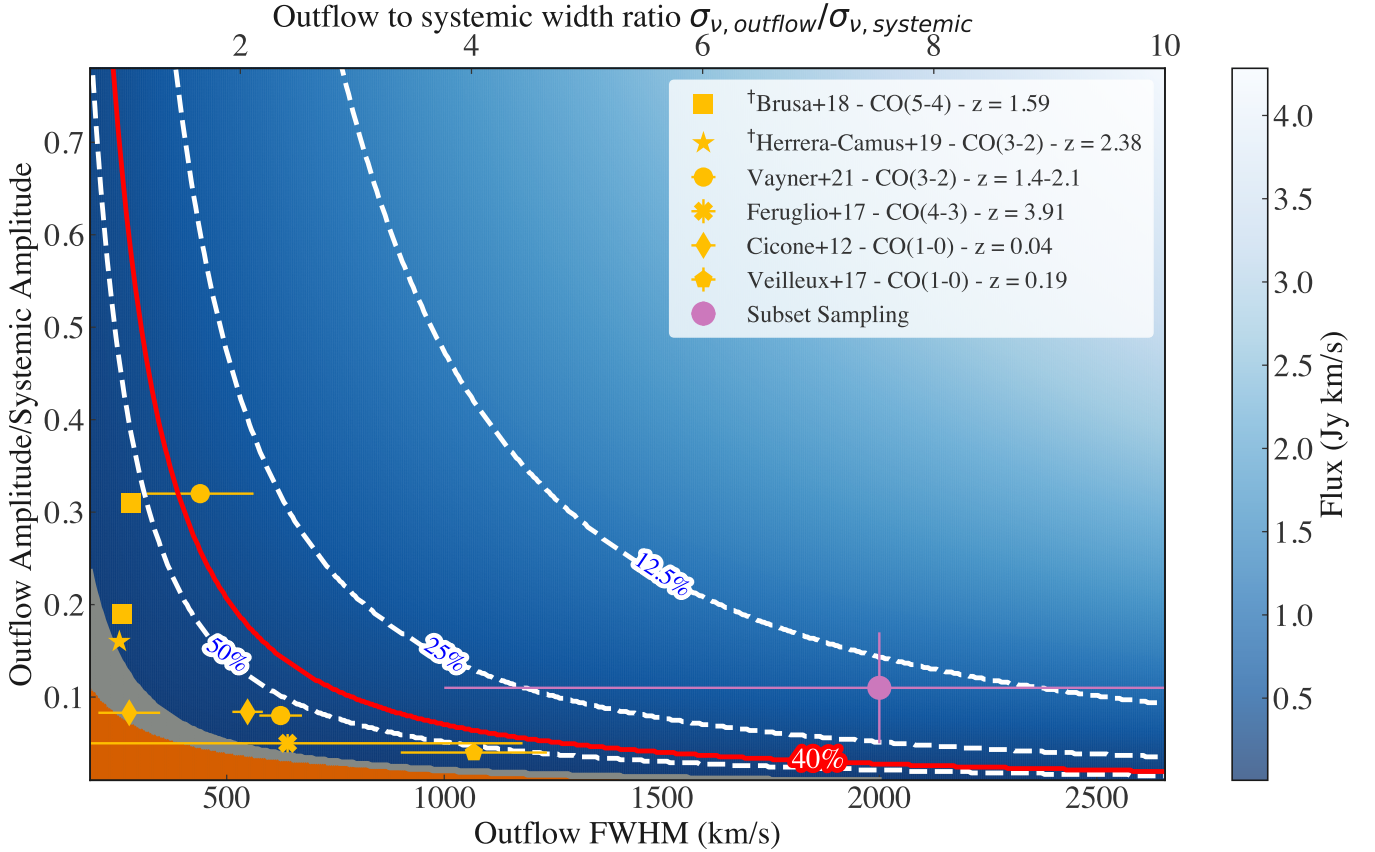


Figure 6. Parameter space of the outflows that, if present, should have been detected by our analysis, based on the upper flux limit and for a range of outflow incidence. The incidence for the sample based on demographics of ionized gas outflows Förster Schreiber et al. (2019), 39.5%, is indicated with the solid bright red line. The grey area delimits the parameter space spanned by outflows below the noise of our stacked spectrum if all sources in the sample have outflows, whereas the orange shaded area shows the flux within the best fit “broad” Gaussian component of the full sample stack, which stands below the noise level. The purple circle indicates the results from the tentative outflow detection in the subset of 41 galaxies with the highest grades. The orange markers indicate outflow properties of molecular outflows identified in bright AGNs/quasars found in the literature (Cicone et al. 2012; Feruglio et al. 2017; Veilleux et al. 2017; Brusa et al. 2018; Herrera-Camus et al. 2019; Vayner et al. 2021). The † symbol marks values reported in the literature but not quoted precisely and/or without errors.

area in Fig. 6. However, previous studies (e.g., Förster Schreiber et al. 2019) report lower incidence values, which also depend on stellar mass, redshift, and SFR. In this case, the stacking of spectra with and without outflow components will “average out” the strength of the potential outflows, decreasing the stacked flux. Consequently, the corresponding maximum flux of outflows in the sample increases as the incidence of outflows decreases. We show this effect by overlaying on the plot upper flux limits com-

puted for incidences of 50%, 25% and 12.5% (dashed white lines). This increases the flux limit as it would require the stacked outflow to have $2\times$, $4\times$, and $8\times$, respectively, the flux of the outflow computed for 100% incidence. Finally, using the ionized gas outflow incidence values from Förster Schreiber et al. (2019), we compute the overall incidence of the sample by taking into account the stellar mass and distance from the main sequence of the galaxies in the sample. This corresponds to an overall

39.5% outflow incidence in the sample of 154 galaxies, plotted in Fig. 6 as the solid red line. In addition, we add to the plot the results from the subset sampling analysis (purple circular marker), where the stack of 41 galaxies reveals a tentative outflow signature. Compared to the full sample, this corresponds to an outflow incidence of 26%, which is in marginal agreement with the upper limits derived from the noise.

For comparison with other molecular gas outflows studies, we also overlay on Fig. 6 the positions of cosmic noon detections of molecular gas outflows in individual galaxies by Feruglio et al. (2017); Brusa et al. (2018); Herrera-Camus et al. (2019) and Vayner et al. (2021), in addition to two local Universe individual detections reported in Cicone et al. (2012) and Veilleux et al. (2017). All but the lowest redshift detection by Cicone et al. (2012) lie above the flux limit for 100% outflow incidence. Unfortunately, very few CO detections of outflows exist at cosmic noon, and all originate from luminous AGNs or QSOs (except for the one reported in Herrera-Camus et al. 2019), which are not representative of the main galaxy population (see Veilleux et al. 2020 for a review).

5. TESTS OF THE METHOD

To check how the different steps of our analysis (see Sec. 3) might influence the results, we redo the analysis on mock data with outflow signatures. This exercise also allows us to quantify limits on the strength and width of a broad outflow component. In addition, we also investigate the potential effects of re-binning on the retrieval of outflow signatures in the stacked spectra.

5.1. Recovery Analysis with Mock Data

5.1.1. Creating Mock Outflows

For this exercise, we create a mock spectrum for individual galaxies employing the single Gaussian best fit to the data, adding a broader

component centered on the narrow component and peak-normalizing the combined narrow+broad (outflow+galaxy) spectrum. Using the blank spectrum extracted for each galaxy to evaluate the noise in each spectrum, we inject realistic (normalized) noise in the mock outflow+galaxy line profile and thus recover a mock galaxy emission line with an outflow component and a SNR comparable to the original data. We also re-bin each spectrum such that the FWHM of the mock outflow+galaxy line covers the same number of channels and stack the resulting spectra following the method described in Sec. 3.3. Finally, we fit the stacks with the same procedure as described in Sec. 4.2. We repeat the process 10,000 times, varying the input outflow amplitude between $0.005-0.8\times$ the narrow component amplitude and the input outflow width between $1-5\times$ the galaxy line width.

For the purpose of this analysis, we choose to add the broad outflow component as centered on the narrow component. That might not be the case, as outflows often show a velocity shift with respect to the narrow emission line. However, when averaging spectra with outflow signatures in the stacking process, the resulting average spectra will display outflow signatures as a broad component centered on the narrow component, hence, we chose to add the broad component already aligned with the narrow component.

5.1.2. Output Flux Recovery

The results are plotted in Fig. 7, which shows, as a function of the input parameters, how well the outflow fluxes are recovered. To make the comparison between the input mock outflows and the retrieved mock outflows, we define the input outflow flux as $F_{\text{input}} = \sqrt{2\pi} \times \overline{A}_{\text{in}} \times \overline{\sigma}_{\text{in}}$ where \overline{A}_{in} is the mean input outflow amplitude over the whole sample and $\overline{\sigma}_{\text{in}}$ is the mean input outflow width over the whole sample, and define the output flux as $F_{\text{output}} = \sqrt{2\pi} \times A_{\text{out}} \times \sigma_{\text{out}}$ where A_{out} is the fitted outflow amplitude after

stacking, and σ_{out} is the fitted outflow width after stacking. From Fig. 7, we observe a clear trend between the strength of the outflow and how well the fitting retrieves the input outflow, as expected. In addition, the width of the outflow seems to have a greater impact on how well the fit performs compared to the amplitude, except for broad-to-narrow amplitude ratios below 0.1. Finally, the excellent recovery (within 20% or better) for sufficiently high flux, broad component amplitude, and σ supports that the re-binning procedure described in Sec. 3.2, which we also apply to all mock spectra before stacking, does not influence the ability to recover a sufficiently strong and wide outflow component.

We note that the fanning up of the distribution at low fluxes is an artifact of the fitting reflecting the difficulty in constraining two components at low fluxes, hence low S/N ratios. Examination of the results shows that in those cases, the formal “best-fit” model is the sum of two Gaussians of very similar amplitude and width (one component with slightly lower amplitude and slightly higher width and *vice versa*, as imposed by the constraints reported in Sec. 4.2). This returns high flux values for the “broad” component, which translates, when computing the ratio of the recovered flux to the input flux, to values much higher than 1.

5.1.3. Comparison with the Real Data

Finally, we compare the analysis of the mock outflows to that of our stacked spectrum from Fig. 2 to determine an upper limit on the broad outflow component. We first consider the flux inside the second “broad” component retrieved in our double Gaussian fit (Sec. 4.2) and identify which mock input outflow properties would reproduce the result we observe with the real data, or return lower flux values (blue diamonds contours in Fig. 7). Similarly, we use the noise of our stacked spectra as an upper limit on the flux of a potential undetected outflow and repeat the same exercise as for the second compo-

nent (solid diamonds in Fig. 7). We conclude that for fluxes below these limits: 1) for the most part, the fit does not recover the “true” input flux, and 2) those flux values correspond either to low values of flux or to outflows with low velocities ($< 1.5\times$ the width of the narrow component).

5.2. Effect of Re-binning on the Stacked Spectra

A possible caveat of the method is re-binning before stacking the spectra. As mentioned in Sec. 3.2, stacking line profiles with a wide range of FWHM can result in the creation of artificial broad wings, which can be misinterpreted as an outflow component. This effect is illustrated in Fig. 8 for the stack of 62 $\Delta\text{MS} > 0.2$ galaxies, where we stack the spectra before and after re-binning to compare the effect of the varying linewidths of the emission lines on the stacked profile. On the other hand, re-binning may reduce the ability to detect a broad component through dilution.

To investigate how re-binning affects the retrieval of outflows in our sample we try varying the values we re-bin the spectra to, which all return similar results to those displayed in Figs. 2 and 4 and where $\Delta\text{BIC} < 0$ favoring a single-Gaussian component fit in all cases. In addition, we also try stacking together subsamples of galaxies with similar linewidths (in which case there is no need for re-binning) and observe no outflow component once again. Since the integrated linewidth can also serve as a proxy for galaxy inclination (for galaxies of the same mass, i.e. rotating at the same velocity, the more inclined galaxies’ line profiles will be wider), the stacking of galaxies with similar linewidths without rebinning also ensures that we do not miss outflows based on inclination.

Finally, the procedure described in Sec. 5 in which we produce mock outflow emission, shows that re-binning does not prevent the fitting from detecting a broad secondary component when

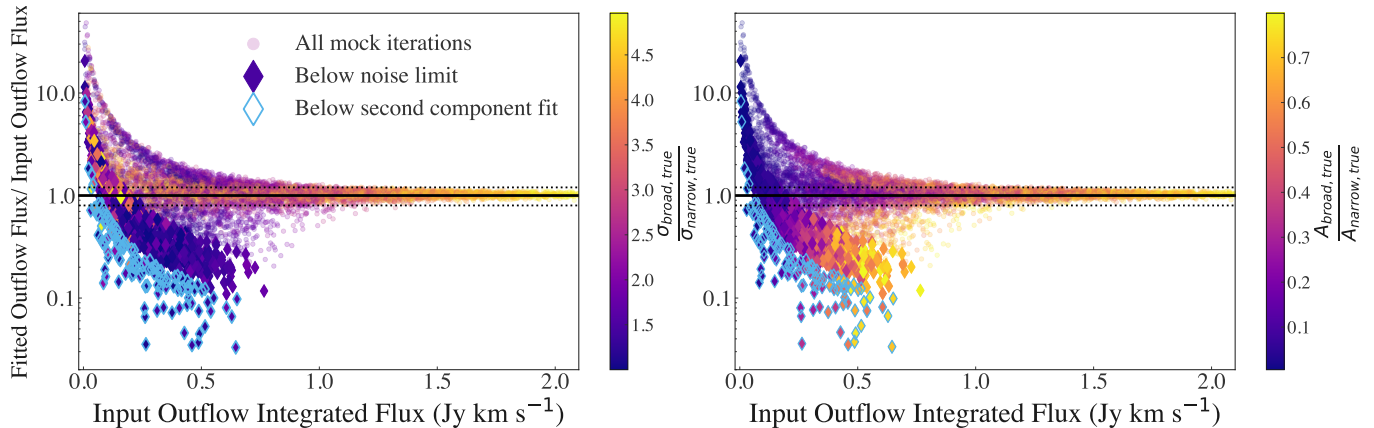


Figure 7. Recovered outflow flux from stacking vs. outflow flux computed from the input parameters for 100,000 mock stacked spectra. The x-axis is converted from normalized flux values to real units using the average amplitudes and velocity binsizes of the stacked spectra. *Left Panel:* Color-coding by the input broad-to-narrow width ratio. *Right Panel:* Same as the left panel, but this time looking at the distribution of the broad-to-narrow amplitude ratio. The solid black line in both panels shows perfect recovery, whereas the two dashed lines mark the area within 20% of this “perfect” fit. The solid diamonds show the iterations where the fitted outflow flux is below the noise of the stacked spectrum. In contrast, the blue diamond contours show the iterations where the fitted mock outflow flux is below the flux of the best fit “broad” Gaussian component of the full sample stack.

a clear signature is present. As a result, if the PHIBSS sample had broad outflow signatures present, which could be revealed by stacking, the re-binning process would not hinder our ability to do so.

6. DISCUSSION

The work presented here investigates the presence of outflows in a sample of 154 SFGs at $0.5 \leq z \leq 2.6$ in a sample representative of the general population. Based on the results presented in Sec. 4, we consider here the physical limits on molecular gas outflows we can retrieve from our stacked spectra, as well as discuss the contribution of various gas phases to outflows.

6.1. Upper limit on Molecular Gas Mass and Mass Outflow Rate

We derive upper limits on outflow properties such as the mass outflow rate and the mass loading factor, for all stacked samples. For the samples for which we do not have an outflow detection, we use as outflow widths and velocities the average values from ionized gas outflows re-

ported in Förster Schreiber et al. (2019), extracted from their stacked spectra. We note that molecular gas outflows traced by CO are generally reported to be slower than their ionized gas counterparts, and thus, these computed values should be interpreted as very conservative upper limits. For the stacked spectrum from the subset sampling analysis in which we have a detection above the noise level (see Sec. 4.4), we define the outflow velocity as $v_{\text{out}} = |\Delta v - 2\sigma_{\text{out}}|$, where Δv is the central velocity differential between the narrow and broad component, and σ_{out} is the width of the best-fit broad component (Veilleux et al. 2005; Genzel et al. 2011, 2014; Concas et al. 2022). All values are reported in Table 1.

To translate the relative limits discussed in the previous subsection into physical limits, we compute the CO line luminosity L'_{CO} in $\text{K km s}^{-1} \text{pc}^2$ using the following relation (Solomon et al. 1997; Veilleux et al. 2017; Tacconi et al. 2020):

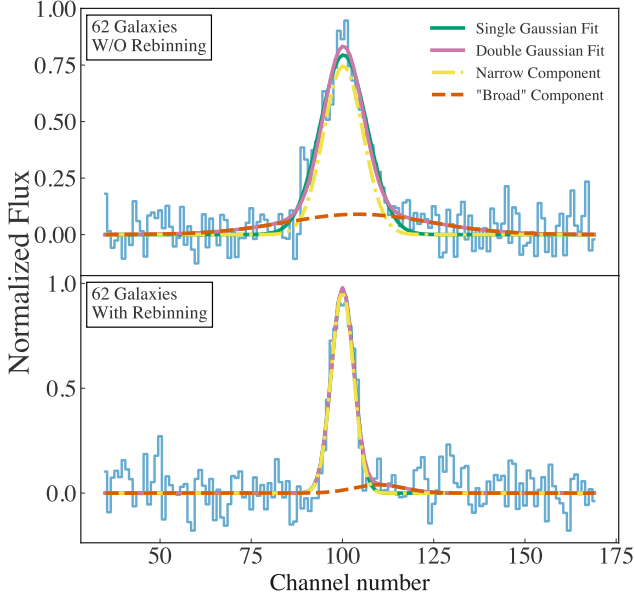


Figure 8. Example plot of the stacking of galaxy spectra without (upper panel) and with (lower) rebinning the individual spectra according to their width pre-stacking. The stacked spectra include the 62 galaxies with $\Delta MS > 0.2$, where we overlay the best fits to the line: solid green is the single component Gaussian, solid purple is the double component Gaussian, and the dashed yellow and orange show the two separate components of the double Gaussian fit. Without rebinning the velocity channels, the stacking induces an artificial broad component mimicking an outflow signature (top panel), which disappears when including the rebinning (bottom panel).

$$L'_{CO} = 3.25 \times 10^7 \cdot S_{CO} \Delta V \cdot \frac{D_L^2}{\nu_{\text{obs}}^2 (1+z)^3}, \quad (1)$$

where the luminosity distance D_L is in Mpc, the observed frequency ν_{obs} is in GHz, and the integrated line flux $S_{CO} \Delta V$ is in Jy km s^{-1} . We use the median values of the galaxies that go into the stacking for the redshift, observed frequency, and luminosity distance.

This luminosity can then be converted into an outflow molecular gas mass estimate:

$$M_{\text{out,mol}} = \alpha_{CO} \cdot \frac{L'_{CO}}{r_{31}} \quad (2)$$

where $r_{31} = 0.77$ is the ratio of temperature brightness to correct for the fact that we are not observing the CO(1-0) transition line but the CO(3-2) (Boogaard et al. 2020), and $\alpha_{CO} = 0.8$ is the ULIRG-like H₂-CO conversion factor in units of $M_{\odot} (\text{K km s}^{-1} \text{ pc}^2)^{-1}$ (Veilleux et al. 2017; Fluetsch et al. 2019). We use the ULIRG α_{CO} in this study, which is commonly used in the literature to obtain the outflow molecular gas mass, but this value relies on the assumption that outflows are well mixed and high metallicity, which might not be the case. Other commonly invoked values of α_{CO} range from 0.3 for the optically thin case (e.g., Bolatto et al. 2013b; Richings & Faucher-Giguère 2018) to 4.3 for the Milky Way value (Bolatto et al. 2013a). Studies in the Local Universe indicate that α_{CO} in outflows is variable from case to case, however the lack of consensus and the resolution of our data does not allow us to take this into account (see Veilleux et al. 2020 for a recent review). Since the molecular gas mass estimate is directly proportional to α_{CO} , this represents one of our estimates' major sources of uncertainty.

Using the estimated molecular gas mass, we can compute an upper limit for the outflowing mass rate, using a simplistic yet plausible assumption commonly used in the literature (e.g., Sturm et al. 2011; Fiore et al. 2017; Herrera-Camus et al. 2019; with the details of the derivation in Rupke et al. 2005):

$$\dot{M}_{\text{out,mol}} = M_{\text{out,mol}} \times \frac{v_{\text{out}}}{R_{\text{out}}} \quad (3)$$

Here, R_{out} is the outermost radius reached by the outflow (we adopt the median effective radius of the galaxies stacked derived from *HST* imaging of the data (Tacconi et al. 2013), by lack of further spatial information and following what was done in Newman et al. 2012b and Förster Schreiber et al. 2019) and v_{out} is the outflow velocity. We compute $\dot{M}_{\text{out,mol}}$ for each stacked sub-sample.

Using this mass outflow rate, we compute the mass loading factor $\eta = \dot{M}_{\text{out}}/\text{SFR}$, where SFR is the median SFR of the sample. The resulting values for each sub-sample are in the ranges $\dot{M}_{\text{out,mol}} = 380 - 2300 M_{\odot}/\text{yr}$ and $\eta_{\text{UL}} = 2.2 - 35.4$. All values and average galaxy properties used for these estimates are reported in Table 1. In all cases, the derived upper limits on the mass loading factor allow for molecular gas outflows to carry a substantial amount of mass, enough to dominate the gas depletion in the galaxy. However, these values rely on numerous assumptions made to yield very conservative upper limits.

6.2. The Gas Phase of Outflows

The vast majority of cold molecular gas outflow detections are in the Local Universe, found in starbursts (Bolatto et al. 2013b; Fluetsch et al. 2019), (U)LIRGs (Lutz et al. 2020; Herrera-Camus et al. 2020b,c; Fluetsch et al. 2021) and AGNs (Cicone et al. 2012; Fiore et al. 2017; Fluetsch et al. 2019; see Harrison & Ramos Almeida 2024 for a recent review). The reported outflow velocities range from a few tens of km/s (Fluetsch et al. 2019) to $> 10^3$ km/s (Fiore et al. 2017; Fluetsch et al. 2019; Lutz et al. 2020), although most have velocities of the order 10^2 km/s (Walter et al. 2002; Bolatto et al. 2013a; Fiore et al. 2017; Fluetsch et al. 2019; Lutz et al. 2020; Krieger et al. 2019). In line with the nearby Universe, the few CO detections at cosmic noon have similar velocities: Brusa et al. (2018) report an outflow detected with velocity ~ 700 km/s, Herrera-Camus et al. (2019) find velocities between $\sim 300 - 500$ km/s, and the quasars in Vayner et al. (2021) host outflows at $\sim 400 - 1100$ km/s. In general, all studies find that molecular gas outflow strength scales with AGN luminosity when one is present. The bulk of the mass budget in the outflows is dominated by the molecular

gas phase, although there are no CO detections of SF-driven outflows at cosmic noon to compare with (see also Langan et al. in prep). In contrast, outflows in warmer gas phases, such as ionized gas, display systematically higher velocities: for AGN-driven outflows, velocities are $\sim 1000 - 2000$ km/s, against a few ~ 100 km/s for SF-driven outflows (Fluetsch et al. 2019; Förster Schreiber et al. 2019; Lutz et al. 2020). With these differences in outflow properties depending on gas phase and power source mechanism, it is not surprising that detecting molecular gas outflows in typical SFGs and low luminosity AGNs at cosmic noon remains a challenge.

However, the challenging nature of the detection may not be the only explanation for the lack of outflow detections in this study. Indeed, the cold molecular phase of outflows might not be the dominant one: most of the outflow could be in a warmer molecular phase as a consequence of energy injection by stellar/AGN feedback in the galactic ISM. In the nearby Universe, studies have already investigated the hot molecular gas phase of outflows ($\gtrsim 1000\text{K}$; e.g., Davies et al. 2014; Ramos Almeida et al. 2019; Riffel et al. 2023) through observations of H_2 rovibrational lines, finding that the AGN could drive tens of Solar masses per year of warm molecular gas, which is unlikely to affect large-scale properties of the host galaxy (Davies et al. 2014). More recently, *JWST*/MIRI has opened the door to the study of warm molecular gas at $\sim 100 - 1000\text{K}$ through purely rotational H_2 lines in the mid-IR, finding low (~ 150 km/s) outflow velocities (Davies et al. 2024a; Dan et al. 2025). In some cases, the molecular gas outflows probed in these local AGNs come from the intersection of the ionised gas outflow with the galactic disk, which perturbs the gas within the galaxy but will not expel it from the galaxy (Ramos Almeida et al. 2022; Davies et al. 2024a).

Sample	$\langle z \rangle$	$\langle \log(M_*/M_\odot) \rangle$	$\langle R_e \rangle$ kpc	$\langle \nu_{\text{obs}} \rangle$ GHz	$\langle \text{SFR} \rangle$ M_\odot/yr	v_{out} km/s	$\dot{M}_{\text{out,mol}}$ M_\odot/yr	η_{UL}
All	1.05	10.8	4.35	136.9	50.1	450 – 2300 [†]	135 – 1567	2.7 – 31.3
AGN	1.09	11.0	3.25	140.6	112.9	1360 [†]	1619	14.3
$M_* > 10^{10.7} M_\odot$	1.01	10.5	4.30	134.2	31.6	420 – 1360 [†]	237 – 1383	3.8 – 21.9
$M_* < 10^{10.7} M_\odot$	1.01	11.0	4.45	140.7	63.1	380 [†]	78	2.5
$\Delta\text{MS} > 0.2$	1.13	10.7	3.60	137.7	79.4	390 – 1500 [†]	373 – 2814	4.7 – 35.4
$\Delta\text{MS} < 0.2$	1.02	10.9	5.00	137.1	31.6	450 – 1520 [†]	85 – 525	2.7 – 16.6
$z > 1.7$	2.21	10.8	3.50	158.5	108.1	460 – 1000 [†]	345 – 1105	2.2 – 6.9
$z < 1.7$	0.76	10.8	5.25	144.0	31.6	460 – 1990 [†]	106 – 956	3.4 – 30.2
Subset Sample	1.01	11.0	5.30	140.7	50.1	1857 ± 905	1528 ± 793	30 ± 16

Table 1. Median properties of the subsamples stacked in Sec. 4.4, and their respective upper limits on mass outflow rates and mass loading factor. Outflow velocities from the ionized gas population trends reported in Förster Schreiber et al. (2019) are marked with a † symbol. In cases where outflow velocities are reported for both SF- and AGN-driven outflows, we use two velocity values corresponding to the average outflow velocity for these subsamples.

The H₂ molecules in the gas could also be dissociated by the galaxies’ radiation fields into atomic hydrogen, particularly in MS galaxies. Using a simple theoretical model, Vijayan & Krumholz (2024) showed that the dissociation of molecular to atomic gas was mostly the result of radiative processes. Consequently, molecular gas in outflows can survive in starburst galaxies, thanks to the combination of denser environments and shorter dynamical times, which allows the molecular gas to escape the galaxy’s radiation field before getting dissociated. In more typical star-forming galaxies, however, the molecules get dissociated, and the cool phase of outflows is mostly composed of atomic gas. In this scenario, the absence of cold molecular gas outflow signatures in our sample might be explained by the fact that the majority of the outflow is in the atomic phase.

The neutral atomic phase of outflows has also been observed, using low-ionization interstellar absorption lines in the rest-UV and optical (e.g., Mg II; Na I D), both in the local Universe (e.g., Rubin et al. 2014; Zhu et al. 2015; Cazzoli et al.

2016; Rupke 2018; Roberts-Borsani & Saintonge 2019; Avery et al. 2022), and at higher redshift (e.g., Shapley et al. 2003; Steidel et al. 2010; Erb et al. 2012; Sugahara et al. 2017). Specifically, using facilities such as *JWST* or Keck/LRIS, studies find prevalent neutral gas outflow signatures in cosmic noon galaxies (Fluetsch et al. 2019, 2021; Kehoe et al. 2024; Davies et al. 2024b; Belli et al. 2024; Taylor et al. 2024). In particular, Belli et al. (2024) find a significant neutral outflow component with velocity ~ 200 km/s in a post-starburst galaxy at $z = 2.45$, which could explain the rapid quenching of star formation in the galaxy. In line with this finding, Davies et al. (2024b) observe neutral outflows through Na I D absorption in $z = 1.7 - 3.5$ galaxies, with velocities 200 – 1100 km/s, which are found in star-forming and quenching systems alike. In a similar ($1.7 < z < 2.7$) redshift range, Kehoe et al. (2024) report neutral outflows detected through low ionization interstellar absorption lines, albeit with lower mean velocities ($\langle \Delta v_{\text{LIS}} \rangle = -56$ km/s). These results indicate that, while the exact properties and im-

pect on galaxy evolution are still uncertain, the neutral gas phase of outflows might play a significant role in the evolution of their host galaxy and represent a major fraction of the outflowing material.

7. CONCLUSION

We present the results from a stacking analysis of the PHIBSS sample, for 154 of galaxies at $0.5 \leq z \leq 2.6$, aiming to detect broad wings that would signal the presence of fast-moving outflowing material. We analyse the full sample and physically motivated sub-samples: above and below $\log(M_*) = 10.7 M_\odot$, above and below $\Delta MS = 0.2$, above and below $z = 1.7$, and identified as AGN. We also perform a bootstrap-like subset sampling analysis to search for a sub-sample with a maximized broad component detection. Reaching integrated SNR > 30 , **we observe no outflow signatures in the full sample or in any of the physically motivated sub-samples (Sec. 4.2) and a 4σ detection in the subset sampling analysis (Sec. 4.4) that could correspond to an outflow signature.** This latter statistically-identified subset represents 26% of the full sample and does not show a clear differentiation in galaxy properties compared to the full sample.

Several factors could impact our ability to recover cold molecular gas outflows despite the use of spectral stacking: 1) a low outflow amplitude and/or low velocities, 2) a low outflow incidence, such that stacking in a larger sample could not reveal their presence (in line with the tentative detection when stacking only a quarter of the full sample), 3) a precise localization of the outflows in the galaxy, such that unresolved studies cannot detect them. The latter two are related to dilution effects of the broad component in a large sample and/or regions where emission is strongly dominated by gravitationally bound gas within the galaxies. However, we note that surface star formation density Σ_{SFR} of the PHIBSS sample follows a similar distribu-

tion to that of KMOS3D, where they detect ionized gas outflows through the stacking of the integrated galaxy spectra (Förster Schreiber et al. 2019). Because of that, we do not expect the absence of molecular gas outflows to be the result of very diluted feedback due to low Σ_{SFR} .

Derived upper limits on the mass outflow rate \dot{M}_{out} and mass loading factor η show that molecular outflows beneath our noise limits could still be more efficient than SF in depleting the gas. We stress that the computed upper limits are very conservative and rely on assumptions (such as the α_{CO}) that may affect the value by factors of > 5 .

In addition, in light of recent searches in alternative tracers at $z \sim 1 - 3$, the dominant phase of outflows in MS galaxies at cosmic noon might not be the cold molecular gas but rather warm molecular gas or neutral atomic gas. However, while outflows in those phases have been detected, there is not currently enough evidence to support either of those phases as the main outflow contributor. To evaluate the mass budget of outflows between the different gas phases at cosmic noon, deeper and higher resolution CO observations, along with observations of various gas tracers, will be needed.

C.B., N.M.F.S., G.T., J.C., J.M.E.S. acknowledge funding by the European Union (ERC, GALPHYS, 101055023). HÜ acknowledges support through the ERC Starting Grant 101164796 “APEX”. Views and opinions expressed are, however, those of the author(s) only and do not necessarily reflect those of the European Union or the European Research Council. Neither the European Union nor the granting authority can be held responsible for them. This work is based on observations carried out with the IRAM PdBI/NOEMA interferometer. IRAM is supported by INSU/CNRS (France), MPG (Germany) and IGN (Spain).

Facilities: PdBI, NOEMA

Software: Astropy (Astropy Collaboration et al. 2013, 2018), SExtractor (Bertin & Arnouts 1996), LINESTACKER (Jolly et al. 2020)

APPENDIX

A. SAMPLE TABLE

This section presents the sample properties for the PHIBSS galaxies used in this analysis with CO line emission detected at integrated SNR > 1.5 (see Table 2). The table does not report the full PHIBSS sample, but only the galaxies with a spectroscopic redshift estimate and lines with SNR > 1.5 . The reported channel size is the channel size after the re-binning process described in Sec. 3.2. In addition, we also present in Fig. 9 the distribution of sample properties, including stellar mass, ΔMS , SNR, inclination, redshift and effective radius. We also plot the distribution of line FWHM, both in km/s and in channels.

Table 2. PHIBSS Sample used in the analysis presented here, including galaxy properties derived from ancillary data. The target names with a dagger are part of the sample stacked and investigated in Sec. 4.4 & Appendix A

Target	R.A.	Decl.	Field	Line	z_{CO}	$\log(M_*/M_\odot)$	ΔMS dex	Type	R_e kpc	FWHM km/s	SNR	Channel Size km/s
EGS13034339	14:20:21.900	+53:02:22.2	EGS	CO(3-2)	1.44	10.8	0.2		3.0	249	5.4	36
XI55	12:37:10.56	+62:11:40.7	GOODS-N	CO(2-1)	0.78802	10.5	0.25		6.6	385	1.2	55
EGS13018632†	14:19:49.100	+52:56:39.2	EGS	CO(3-2)	1.229	10.7	0.25		1.9	221	3.73	32
XF53†	09:58:33.86	+02:19:50.9	COSMOS	CO(2-1)	0.50198	11.1	0.08		6.9	546	2.08	78
L14GN008	12:36:07.83	+62:12:00.6	GOODS-N	CO(2-1)	0.50276	10.3	-0.27		6.4	160	3.01	23
L14CO004	10:00:40.29	+02:20:32.6	COSMOS	CO(2-1)	0.68822	10.5	-0.15			360	3.5	51
EGS13034541	14:20:22.200	+53:02:14.8	EGS	CO(3-2)	1.442	10.97	0.51		8.0	435	6.33	62
EGS13011148	14:19:29.810	52:53:13.130	EGS	CO(3-2)	1.173	11.0	-0.1		5.5	384	4.69	55
L14GN014	12:36:51.82	+62:15:04.7	GOODS-N	CO(3-2)	2.19044	10.6	0.23	AGN	2.0	283	1.23	40
L14EG013†	14:19:17.33	+52:50:35.3	EGS	CO(2-1)	0.65855	11.1	0.48	AGN	8.5	353	4.81	50
XA55	12:36:59.92	+62:14:50.0	GOODS-N	CO(2-1)	0.7609	10.5	0.65		4.0	126	3.35	18
EGS12028325	14:18:59.200	+52:47:16.9	EGS	CO(3-2)	1.159	10.4	0.43		3.3	178	5.81	25
L14GN035†	12:36:35.60	+62:14:24.0	GOODS-N	CO(6-5)	2.01399	11.5	0.52	AGN	7.7	616	2.54	88
XU53	10:00:40.37	+02:23:23.6	COSMOS	CO(2-1)	0.51638	10.3	0.43		6.8	262	1.7	37
L14EG010	14:20:22.80	+52:55:56.3	EGS	CO(2-1)	0.66944	10.7	-0.13		2.6	27	10.11	4
L14EG011	14:20:26.20	+52:57:04.9	EGS	CO(2-1)	0.57094	10.7	0.27		9.7	405	3.19	58
L14CO027	10:00:45.00	+02:07:05.1	COSMOS	CO(3-2)	2.16887	10.3	0.45		3.6	100	5.4	14
L14CO026†	09:59:55.85	+02:06:50.2	COSMOS	CO(3-2)	2.18079	10.4	0.77		3.6	6	8.67	1
Q2343-MD59	23:46:26.900	12:47:39.870	other	CO(3-2)	2.011	10.9	-0.66		7.4	216	3.02	31
L14EG018	14:19:38.67	+52:51:38.8	EGS	CO(6-5)	2.325	11.5	0.42		4.5	56	2.89	8
XI55	12:36:17.33	+62:12:12.8	GOODS-N	CO(3-2)	1.01779	11.2	-0.48		5.8	102	2.09	15
XI54†	14:19:40.94	+52:51:57.2	EGS	CO(3-2)	1.0125	11.5	-0.67		7.8	337	2.59	48
HDF-BX1439	12:36:53.660	62:17:24.270	GOODS-N	CO(3-2)	2.187	10.8	-0.1		4.1	279	1.81	40
EGS13011155†	14:19:41.600	+52:52:56.5	EGS	CO(3-2)	1.012	11.1	0.46	AGN	7.8	470	5.37	67
L14GN009	12:36:18.50	+62:09:03.5	GOODS-N	CO(3-2)	1.67551	11.4	-0.6		4.2	97	6.5	14
L14GN021†	12:36:03.26	+62:11:11.0	GOODS-N	CO(2-1)	0.63836	10.7	0.77		1.2	373	7.8	53
L14GN020	12:36:18.29	+62:08:19.6	GOODS-N	CO(2-1)	1.01748					277	2.92	40
L14CO005†	10:00:28.70	+02:17:45.4	COSMOS	CO(3-2)	2.09946	11.3	-0.38	AGN	2.1	181	2.6	26
XD54	14:19:46.35	+52:54:37.2	EGS	CO(2-1)	0.75471	10.4	0.49		3.2	207	5.03	30

Table 2 *continued*

Table 2 (continued)

Target	R.A.	Decl.	Field	Line	z_{CO}	$\log(M_*/M_\odot)$	ΔMS	Type	R_e	FWHM	SNR	Channel Size
							dex	kpc	km/s	km/s		km/s
XD55	12:36:21.04	+62:12:08.5	GOODS-N	CO(2-1)	0.77927	10.5	0.25			218	3.1	31
EGS12012083	14:17:56.790	52:32:00.290	EGS	CO(3-2)	1.119	11.0	0.3	4.4	4.4	576	3.67	82
EGS12023832	14:19:06.100	+52:43:12.3	EGS	CO(3-2)	1.351	10.8	0.4	4.7	4.7	395	2.26	56
L14CO012	10:00:45.53	+02:33:39.6	COSMOS	CO(2-1)	0.70074	10.6	-0.09	4.4	4.4	53	5.61	8
EGS13019114 [†]	14:19:41.100	+52:56:16.3	EGS	CO(3-2)	1.105	10.8	-0.0	7.2	7.2	419	6.38	60
L14CO016 [†]	10:00:11.16	+02:35:41.6	COSMOS	CO(2-1)	0.69648	11.0	0.2	3.4	3.4	228	2.71	33
XK53	10:01:59.05	+01:46:58.1	COSMOS	CO(3-2)	2.024	10.5	0.2	1.4	1.4	29	8.83	4
L14GN003	12:36:11.52	+62:10:33.6	GOODS-N	CO(3-2)	2.24344	11.3	0.12	5.6	5.6	807	1.82	115
L14GN002	12:36:44.83	+62:17:16.0	GOODS-N	CO(3-2)	2.03182	10.8	0.1	3.8	3.8	128	4.36	18
EGS12004280	14:17:00.900	+52:27:01.3	EGS	CO(3-2)	1.023	10.6	0.41	4.7	4.7	211	3.5	30
Q1700-BX691	17:01:06.000	64:12:10.270	other	CO(3-2)	2.189	10.9	-0.36	4.0	4.0	208	2.25	30
XC53 [†]	10:00:58.20	+01:45:59.0	COSMOS	CO(2-1)	0.61686	10.9	0.52	AGN		118	2.78	17
Q1700-MD94	17:00:42.020	64:11:24.220	other	CO(3-2)	2.333	11.2	0.17	2.8	2.8	468	6.86	67
L14EG007 [†]	14:19:19.01	+52:48:30.5	EGS	CO(2-1)	1.5274			AGN		71	3.41	10
L14EG006	14:18:45.52	+52:43:24.1	EGS	CO(2-1)	0.50148	10.5	-0.15	8.0	8.0	71	8.34	10
L14CO018	10:00:58.20	+01:45:59.0	COSMOS	CO(2-1)	0.61686	10.9	0.52	AGN		515	3.07	74
L14GN015	12:36:43.19	+62:11:48.0	GOODS-N	CO(2-1)	1.00996	10.9	-0.45	5.3	5.3	216	3.66	31
Q1700-MD174	17:00:54.540	64:16:24.760	other	CO(3-2)	2.34	11.4	-0.13	4.0	4.0	834	3.3	119
L14CO003	10:00:43.81	+02:14:09.2	COSMOS	CO(3-2)	2.18195	10.6	0.33	3.1	3.1	36	6.23	5
L14CO002	10:00:16.43	+02:23:00.8	COSMOS	CO(3-2)	2.18422	10.5	0.6	1.3	1.3	89	3.49	13
XD53 [†]	10:01:58.73	+02:15:34.2	COSMOS	CO(2-1)	0.70203	10.9	0.42	3.4	3.4	393	5.17	56
EGS12020405	14:18:04.990	52:40:25.290	EGS	CO(3-2)	1.379	10.6	0.61	7.4	7.4	437	2.79	62
Q1623-BX528	16:25:56.440	26:50:15.440	other	CO(3-2)	2.268	10.8	-0.2	4.6	4.6	56	3.64	8
L14GN030	12:36:25.30	+62:10:35.6	GOODS-N	CO(3-2)	2.08236	11.0	-0.12	3.8	3.8	499	5.53	71
L14GN018	12:36:31.66	+62:16:04.1	GOODS-N	CO(2-1)	0.78317	10.4	0.49	3.4	3.4	179	5.47	26
HDF-BX1439 [†]	14:19:09.500	52:53:06.400	EGS	CO(3-2)	1.099	10.9	0.05	2.4	2.4	111	5.69	16
Q1700-BX561	17:01:04.180	64:10:43.830	other	CO(3-2)	2.434			1.0	1.0	235	2.25	34
L14GN004	12:37:04.34	+62:14:46.2	GOODS-N	CO(3-2)	2.2143	10.7	0.37	AGN		296	4.22	42
L14GN005 [†]	12:37:20.05	+62:12:22.8	GOODS-N	CO(3-2)	2.46026	10.8	0.4	2.8	2.8	144	4.24	21
L14CO021 [†]	10:00:24.70	+02:29:12.1	COSMOS	CO(2-1)	0.70155	11.5	0.07	2.5	2.5	334	2.71	48
XK55	12:36:46.19	+62:11:42.1	GOODS-N	CO(3-2)	1.01578	11.4	-0.25	9.8	9.8	284	2.7	41
XC55	12:36:09.76	+62:14:22.6	GOODS-N	CO(2-1)	0.78013	10.7	0.37	2.9	2.9	289	5.91	41
XC54 [†]	14:19:49.14	+52:52:35.8	EGS	CO(2-1)	0.50933	11.3	0.37	14.6	14.6	688	2.12	98

Table 2 continued

Table 2 (continued)

Target	R.A.	Decl.	Field	Line	z_{CO}	$\log(M_*/M_\odot)$	ΔMS	Type	R_e	FWHM	SNR	Channel Size
							dex		kpc	km/s		km/s
EGS13011166 [†]	14:19:45	+52:52:28.0	EGS	CO(3-2)	1.529	11.1	0.07		6.5	14	5.63	2
XW53	10:00:45.52	+02:16:34.3	COSMOS	CO(2-1)	0.74949	10.4	0.09			89	2.53	13
L14GN019 [†]	12:36:29.02	+62:09:48.1	GOODS-N	CO(3-2)	2.31475					40	2.84	6
EGS13034445	14:20:30.800	53:01:48.500	EGS	CO(3-2)	1.168	11.1	-0.34		3.8	299	3.29	43
XL53 [†]	10:00:28.27	+02:16:00.5	COSMOS	CO(2-1)	0.74848	11.2	0.27		1.6	42	6.17	6
XR53	10:01:41.85	+02:07:09.8	COSMOS	CO(2-1)	0.51685	11.3	-0.03			176	4.01	25
L14GN026	12:36:36.74	+62:17:47.8	GOODS-N	CO(3-2)	2.21233					26	9.11	4
XF55 [†]	12:35:55.43	+62:10:56.8	GOODS-N	CO(2-1)	0.6381	10.2	0.08		6.9	408	2.76	58
XF54 [†]	14:19:41.70	+52:55:41.3	EGS	CO(2-1)	0.76832	10.8	0.14		6.2	218	3.64	31
XA53 [†]	10:02:02.09	+02:09:37.4	COSMOS	CO(2-1)	0.69861	11.5	0.47		10.1	458	4.91	65
L14GN013	12:37:00.46	+62:15:08.9	GOODS-N	CO(3-2)	2.32941	11.1	-0.18	AGN	1.8	282	3.91	40
L14GN012 [†]	12:37:07.20	+62:14:08.1	GOODS-N	CO(3-2)	2.48614	11.3	-0.08	AGN	4.0	539	6.39	77
Q1623-BX599	16:26:02.540	26:45:31.900	other	CO(3-2)	2.33	10.8	0.1		1.0	98	7.13	14
EGS13004661	14:18:40.840	52:48:35.650	EGS	CO(3-2)	1.192	10.5	0.27		6.3	496	1.98	71
L14EG016	14:18:28.90	+52:43:05.3	EGS	CO(2-1)	0.64418					228	2.77	33
EGS13004684 [†]	14:18:55.800	+52:47:49.5	EGS	CO(3-2)	1.014	11.0	-0.2		5.0	353	2.63	51
L14CO008 [†]	09:58:09.07	+02:05:29.8	COSMOS	CO(2-1)	0.60674	10.9	-0.08			196	5.39	28
L14CO020	11:24:15.64	-21:39:31.0	COSMOS	CO(3-2)	2.38257					31	7.04	4
L14CO009	09:58:56.45	+02:08:06.7	COSMOS	CO(2-1)	0.69763	10.5	0.25		5.8	273	3.65	39
EGS13004291	14:19:15	+52:49:29.9	EGS	CO(3-2)	1.145	10.97	1.01	AGN	3.1	335	23.17	48
XE55	12:36:11.26	+62:14:20.9	GOODS-N	CO(2-1)	0.76796	10.5	0.15		5.2	176	4.4	25
XE54	14:19:35.27	+52:52:49.9	EGS	CO(2-1)	0.50945	10.4	-0.01		8.2	277	4.71	40
EGS13017614	14:20:24.300	52:55:41.300	EGS	CO(3-2)	1.18	11.1	0.06		5.9	360	8.26	51
Q2346-BX482	23:48:12.969	00:25:46.336	other	CO(3-2)	2.264	9.8	0.26		3.8	185	3.86	26
EGS12011767	14:18:24.710	52:32:55.250	EGS	CO(3-2)	1.282	10.5	0.37		6.0	133	6.98	19
L14CO019 [†]	10:00:35.69	+02:31:15.6	COSMOS	CO(2-1)	0.6777	10.9	0.22		14.9	122	3.54	17
EGS13042293	14:20:40.800	+53:04:59.2	EGS	CO(3-2)	1.393	10.6	0.11		5.2	195	6.11	28
EGS13003805 [†]	14:19:40.070	52:49:38.560	EGS	CO(3-2)	1.23	11.2	0.42	AGN	5.6	409	9.12	58
XO53 [†]	10:02:51.41	+02:18:49.7	COSMOS	CO(2-1)	0.60681	11.4	-0.14	AGN	1.1	194	3.41	28
EGS12004351	14:17:02	+52:26:58.5	EGS	CO(3-2)	1.017	10.9	0.45		5.7	537	6.77	77
L14GN016	12:37:22.94	+62:14:19.7	GOODS-N	CO(2-1)	1.02173	11.4	-0.25		5.2	37	5.62	5
L14GN022	12:36:36.76	+62:11:56.1	GOODS-N	CO(2-1)	0.55611	10.1	-0.06	AGN	1.0	93	2.4	13
L14CO006	10:00:31.08	+02:12:25.9	COSMOS	CO(3-2)	2.30902	10.6	-0.17		4.1	477	3.43	68

Table 2 continued

Table 2 (continued)

Target	R.A.	Decl.	Field	Line	z_{CO}	$\log(M_*/M_\odot)$	ΔMS	Type	R_e	FWHM	SNR	Channel Size
							dex		kpc	km/s		km/s
L14CO022	10:01:47.00	+02:23:25.0	COSMOS	CO(3-2)	2.208	10.3	0.45		2.0	80	5.26	11
EGS13019128	14:19:38.100	+52:55:40.9	EGS	CO(3-2)	1.35	10.6	0.31		5.2	194	7.77	28
Q2343-BX513	23:46:11.130	12:48:32.140	other	CO(3-2)	2.109	10.4	-0.33		4.0	134	2.2	19
XH55	12:37:13.87	+62:13:35.0	GOODS-N	CO(2-1)	0.77839	10.3	0.13		5.5	275	4.69	39
XH54	14:19:45.42	+52:55:51.0	EGS	CO(2-1)	0.75573	10.2	0.18		5.4	74	3.91	11
X453	16:25:50.850	26:49:31.300	other	CO(3-2)	2.182	10.5	0.6		2.0	230	5.17	33
L14CO011	10:00:14.30	+02:30:47.2	COSMOS	CO(2-1)	0.69685	10.4	0.49		1.9	286	7.53	41
L14EG005	14:18:59.76	+52:42:50.8	EGS	CO(3-2)	2.16865	10.6	0.03		16.1	282	2.57	40
EGS13034542	14:20:21.200	+02:05:04.2	EGS	CO(3-2)	1.435	10.7	0.15		4.0	13	8.79	2
EGS13035123	14:20:05.500	53:01:15.600	EGS	CO(3-2)	1.115	11.2	0.02		9.1	121	10.61	17
L14GN017†	12:36:53.66	+62:17:24.3	GOODS-N	CO(3-2)	2.18711	10.5	0.2		3.4	180	2.96	26
EGS13017973	14:20:13.100	+52:56:13.7	EGS	CO(3-2)	1.031	10.6	0.11		7.2	78	7.62	11
L14GN029	12:37:28.10	+62:14:40.0	GOODS-N	CO(3-2)	2.54866					35	10.1	5
L14CO013	10:02:16.78	+01:37:25.0	COSMOS	CO(2-1)	0.62109	11.2	0.07	AGN	1.9	458	2.71	66
L14CO025	09:59:57.20	+02:12:25.2	COSMOS	CO(3-2)	2.45796	11.0	0.08			86	6.77	12
L14EG012	14:19:52.95	+52:51:11.1	EGS	CO(2-1)	0.54413	11.1	-0.22		15.3	165	3.81	24
EGS13018076	14:20:10.800	+52:53:41.5	EGS	CO(3-2)	1.227	11.0	0.1		8.0	87	4.59	12
XT53	10:01:39.31	+02:17:25.8	COSMOS	CO(2-1)	0.70096	11.1	0.18			265	3.72	38
L14CO010†	10:01:08.69	+01:44:28.2	COSMOS	CO(3-2)	2.23988	11.2	0.07			343	2.5	49
L14GN034†	12:36:19.68	+62:19:08.1	GOODS-N	CO(2-1)	0.51939	10.9	-0.28		9.6	753	2.94	108
EGS13018312	14:19:58.300	+52:55:49.4	EGS	CO(3-2)	1.105	10.8	-0.2		4.0	251	6.99	36
L14GN023	12:36:00.14	+62:10:47.2	GOODS-N	CO(3-2)	1.99909	10.8	0.47	AGN	0.6	237	2.06	34
L14CO007†	10:00:25.18	+02:29:53.9	COSMOS	CO(2-1)	0.50185	10.7	-0.53		10.7	385	3.92	55
EGS12015684	14:18:42.090	52:36:20.160	EGS	CO(3-2)	1.374	10.7	0.45		3.8	106	9.07	15
L14EG002	14:19:27.42	+52:47:55.6	EGS	CO(3-2)	2.29574	11.0	0.18		1.9	99	3.77	14
EGS13026117	14:20:26.500	+52:59:39.6	EGS	CO(3-2)	1.241	11.1	0.26		3.2	168	20.87	24
L14EG003	14:19:15.35	+52:44:31.7	EGS	CO(3-2)	2.02781	10.9	0.24		2.5	203	3.23	29
L14GN010†	12:36:41.42	+62:11:42.5	GOODS-N	CO(3-2)	1.52663	11.2	-0.49		6.8	699	6.32	100
L14GN011	12:37:22.53	+62:18:38.2	GOODS-N	CO(3-2)	1.52315	11.5	-0.55		10.8	426	3.77	61
XM53	10:01:53.57	+01:54:14.8	COSMOS	CO(2-1)	0.70033	11.6	0.17		2.1	648	3.28	93
EGS13033731	14:20:43.300	+53:03:48.5	EGS	CO(3-2)	1.317	10.4	-0.07		5.5	87	2.42	12
L14GN006	12:36:34.41	+62:17:50.5	GOODS-N	CO(2-1)	0.68333	10.5	0.35		4.3	323	3.75	46
L14GN007	12:36:32.38	+62:07:34.1	GOODS-N	CO(2-1)	0.59423	10.8	-0.26		6.1	441	4.59	63

Table 2 continued

Table 2 (*continued*)

Target	R.A.	Decl.	Field	Line	z_{CO}	$\log(M_*/M_\odot)$	ΔMS	Type	R_e	FWHM	SNR	Channel Size
							dex		kpc	km/s		km/s
EGS13017843	14:20:18.900	+52:56:05.1	EGS	CO(3-2)	1.052	10.6	-0.09		4.2	518	3.35	74
L14CO023	10:01:59.05	+01:46:58.1	COSMOS	CO(3-2)	2.024	10.5	0.2		1.4	57	6.06	8
XG54	14:20:13.43	+52:54:05.9	EGS	CO(2-1)	0.65935	11.3	-0.03		13.0	287	5.81	41
L14GN028	12:37:02.93	+62:14:23.6	GOODS-N	CO(2-1)	0.51138	10.8	-0.26		5.0	278	5.37	40
L14EG014	14:20:33.58	+52:59:17.5	EGS	CO(2-1)	0.71013	10.9	-0.38	AGN	4.5	119	3.59	17
L14EG015	14:20:45.61	+53:05:31.2	EGS	CO(2-1)	0.73785	11.0	-0.1		1.2	57	5.49	8
EGS12004754	14:16:42.100	52:25:19.100	EGS	CO(3-2)	1.026	11.0	-0.1		5.0	88	6.74	12
Q2343-BX610 [†]	23:46:09.430	12:49:19.210	other	CO(3-2)	2.211	11.0	0.18		4.0	256	15.26	37
Q2343-BX442	23:46:19.360	12:47:59.690	other	CO(3-2)	2.175	11.1	0.02		2.0	291	2.3	42
L14GN033 [†]	12:36:53.81	+62:08:27.7	GOODS-N	CO(2-1)	0.56117	10.1	-0.06		6.7	51	3.44	7
Q1700-MD69	17:00:47.620	64:09:44.780	other	CO(3-2)	2.289	11.3	-0.08		4.6	178	6.57	25
L14EG017	14:19:49.28	+52:51:34.1	EGS	CO(6-5)	2.18691	10.9	0.24	AGN	1.4	318	2.35	45
L14GN024	12:37:23.47	+62:17:20.2	GOODS-N	CO(3-2)	2.22332	10.6	0.23		4.2	114	4.23	16
L14CO001	10:00:18.91	+02:18:10.1	COSMOS	CO(2-1)	0.50214	10.2	0.58		7.2	166	4.9	24
XF53	10:01:00.74	+01:49:53.0	COSMOS	CO(2-1)	0.52892	10.4	0.39		2.0	240	5.16	34
EGS13017707 [†]	14:20:13	+52:55:34.0	EGS	CO(3-2)	1.037	10.87	0.76	AGN	3.6	304	5.39	43
EGS12024866	14:18:19.270	52:42:21.520	EGS	CO(3-2)	1.002	10.4	0.03		4.4	215	3.71	31
L14GN025	12:37:13.99	+62:20:36.6	GOODS-N	CO(2-1)	0.53281	10.7	-0.63		1.9	229	1.58	33
XJ55 [†]	12:36:29.13	+62:10:46.1	GOODS-N	CO(3-2)	1.01418	11.4	0.15	AGN	8.5	1025	5.27	146
L14CO014	10:01:09.67	+02:30:00.7	COSMOS	CO(2-1)	0.7019	10.7	0.17		0.6	119	4.66	17
XV53 [†]	10:01:43.66	+02:48:09.4	COSMOS	CO(2-1)	0.62351	10.8	0.24		1.6	489	4.45	70
L14EG009 [†]	14:20:04.88	+52:59:38.8	EGS	CO(2-1)	0.73586	10.1	0.14		3.0	211	3.66	30
L14EG008	14:19:39.46	+52:52:33.6	EGS	CO(2-1)	0.7316	10.9	0.72		7.9	234	10.43	33
XB54	14:19:37.26	+52:51:03.4	EGS	CO(2-1)	0.66997	11.4	0.26	AGN	37.9	84	8.13	12
XB55	12:36:08.13	+62:10:35.9	GOODS-N	CO(2-1)	0.6791			AGN		20	4.52	3

B. INDIVIDUAL SPECTRA INVESTIGATION

Three objects are discussed in Sec. 4.1, as they display asymmetries in the line profile. For two of them (EGS13035123 and EGS12004351), correcting the mask used to extract the spectra is enough to change the asymmetry to the double-peaked profile indicative of galactic rotation. Fig. 10 shows the spectra of one of these galaxies, EGS13035123, before and after adjusting the mask.

In contrast, in the case of EGS13003805 (Fig. 11), the spectrum retains its asymmetric shape even when changing the aperture. Based on the strength of the asymmetric feature and through visual inspection of the cube, we believe that the feature is still a signature of rotation.

C. EXTENDED AND ANNULI APERTURES

As described in Sec. 4.3, we performed the spectral stacking analysis not only on spectra extracted from the smallest possible aperture but also on spectra from apertures wider by 10 kpc (following the outflow detection in [Herrera-Camus et al. 2019](#)), as well as on "annuli" apertures of only the additional 10kpc around the original aperture. The goal is to search extended emission in the galaxy and potential outflow signatures in the outskirts of the galaxies.

The resulting spectra for the extended and annuli apertures are shown in Fig. 12, along with the best-fit single Gaussian, and the fit residuals. Similar to Fig. 2 and 4, both the spectra and fit residuals show no indication of a broad secondary outflow component. Additional fitting of a double Gaussian model does not improve the residuals, or the goodness-of-fit (verified through a reduced χ^2 and ΔBIC analysis).

D. SUBSET SAMPLING INVESTIGATION

As part of the subset sampling analysis presented in Sec. 4.4, we investigate the subsample of 41 galaxies with the highest grade, which also presents signs of a tentative outflow detection (marker with a † symbol in Table 2). As such we compare the galaxy properties of the subsample to that of the full sample (see Fig. 13) and see that there are no clear distinction in the distribution of data and galaxy properties. The SNR and ΔMS distributions have almost the same median, and the subsample median is at slightly lower redshift compared to that of the full sample (1.012 vs 1.099, respectively). The only noticeable difference in sample properties is the median stellar mass, which is $10^{10.8} M_{\odot}$ for the full sample, and $10^{10.95} M_{\odot}$ for the subsample. In addition, 13 of these 41 galaxies are identified as AGN (see Sec. 2.2), which gives an AGN incidence of 32% in this subsample, as opposed to 16% in the full sample.

REFERENCES

- Astropy Collaboration, Robitaille, T. P., Tollerud, E. J., et al. 2013, *A&A*, 558, A33, doi: [10.1051/0004-6361/201322068](https://doi.org/10.1051/0004-6361/201322068)
- Astropy Collaboration, Price-Whelan, A. M., Sipőcz, B. M., et al. 2018, *AJ*, 156, 123, doi: [10.3847/1538-3881/aabc4f](https://doi.org/10.3847/1538-3881/aabc4f)
- Avery, C. R., Wuyts, S., Förster Schreiber, N. M., et al. 2021, *MNRAS*, 503, 5134, doi: [10.1093/mnras/stab780](https://doi.org/10.1093/mnras/stab780)
- . 2022, *MNRAS*, 511, 4223, doi: [10.1093/mnras/stac190](https://doi.org/10.1093/mnras/stac190)
- Baldwin, J. A., Phillips, M. M., & Terlevich, R. 1981, *PASP*, 93, 5, doi: [10.1086/130766](https://doi.org/10.1086/130766)
- Belli, S., Park, M., Davies, R. L., et al. 2024, *Nature*, 630, 54, doi: [10.1038/s41586-024-07412-1](https://doi.org/10.1038/s41586-024-07412-1)
- Bertin, E., & Arnouts, S. 1996, *A&AS*, 117, 393, doi: [10.1051/aas:1996164](https://doi.org/10.1051/aas:1996164)
- Bolatto, A. D., Wolfire, M., & Leroy, A. K. 2013a, *ARA&A*, 51, 207, doi: [10.1146/annurev-astro-082812-140944](https://doi.org/10.1146/annurev-astro-082812-140944)

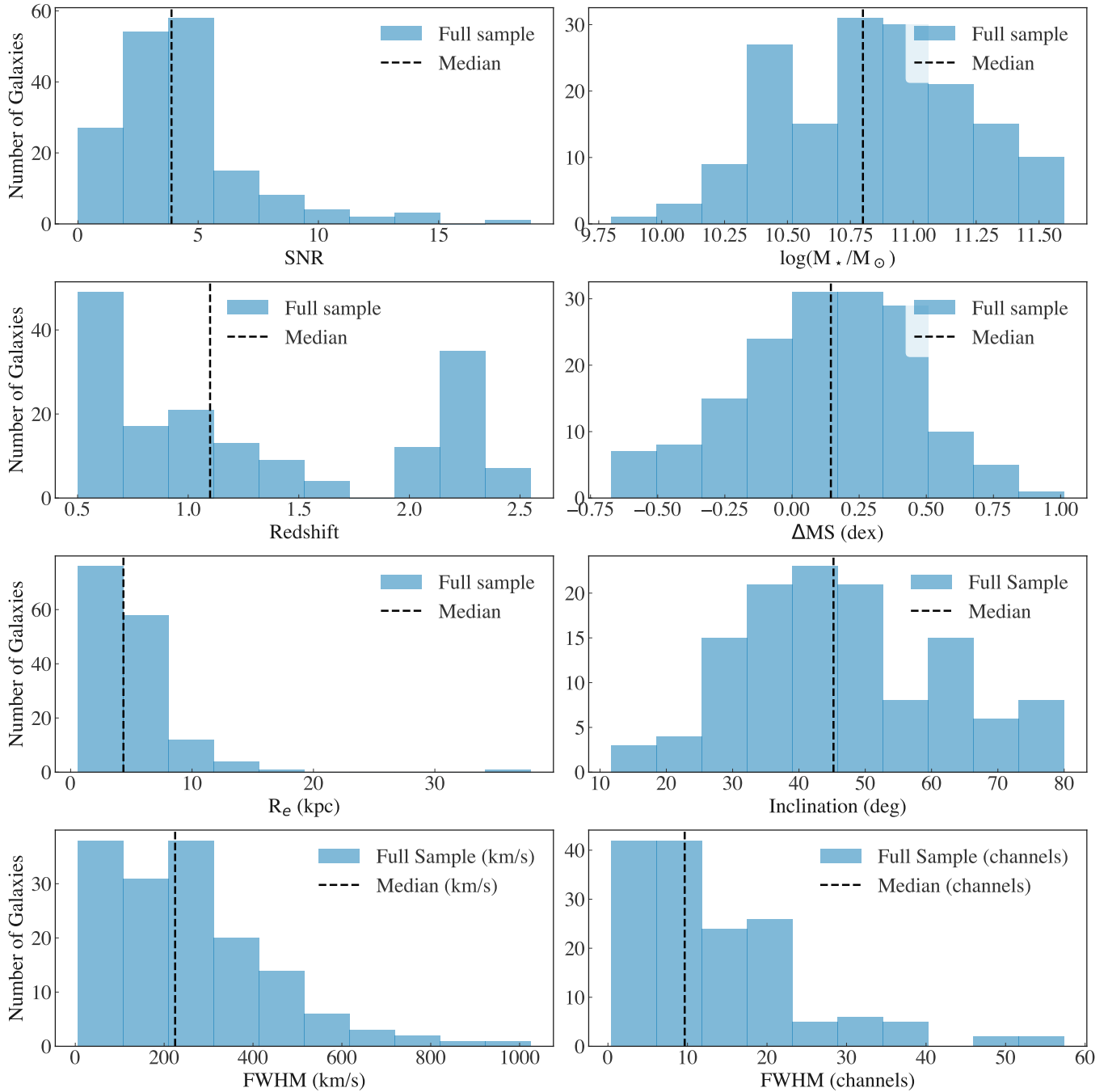


Figure 9. Distributions of the full sample’s properties. The black dashed line in each panel indicates the median value. The FWHM distribution is plotted twice, in channels and km/s.

Bolatto, A. D., Warren, S. R., Leroy, A. K., et al. 2013b, *Nature*, 499, 450, doi: [10.1038/nature12351](https://doi.org/10.1038/nature12351)

Boogaard, L. A., van der Werf, P., Weiss, A., et al. 2020, *ApJ*, 902, 109, doi: [10.3847/1538-4357/abb82f](https://doi.org/10.3847/1538-4357/abb82f)

Brusa, M., Cresci, G., Daddi, E., et al. 2018, *A&A*, 612, A29, doi: [10.1051/0004-6361/201731641](https://doi.org/10.1051/0004-6361/201731641)

Calabrò, A., Pentericci, L., Talia, M., et al. 2022, *A&A*, 667, A117, doi: [10.1051/0004-6361/202244364](https://doi.org/10.1051/0004-6361/202244364)

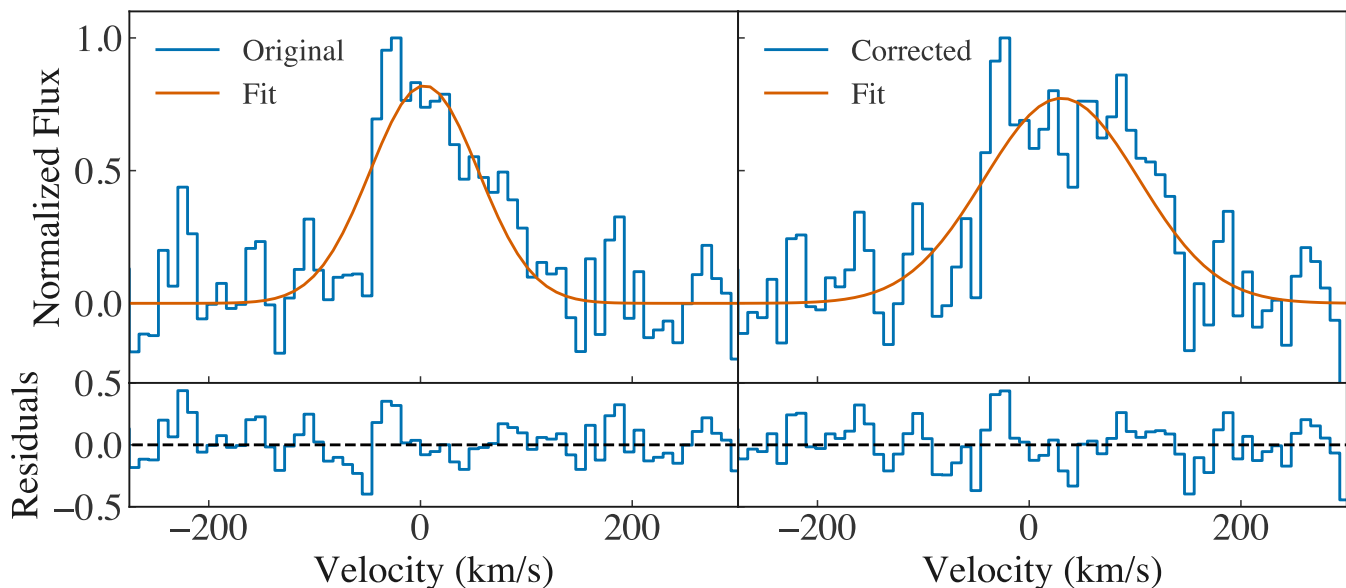


Figure 10. Example of a high SNR spectrum (blue curve) in EGS13035123 showing asymmetry in the CO(3-2) line profile (left panel), and how the line shape changes when correcting the aperture mask (right). Overlaid are the best-fit Gaussian profiles (orange lines), and the bottom panels show the fit residuals in both cases.

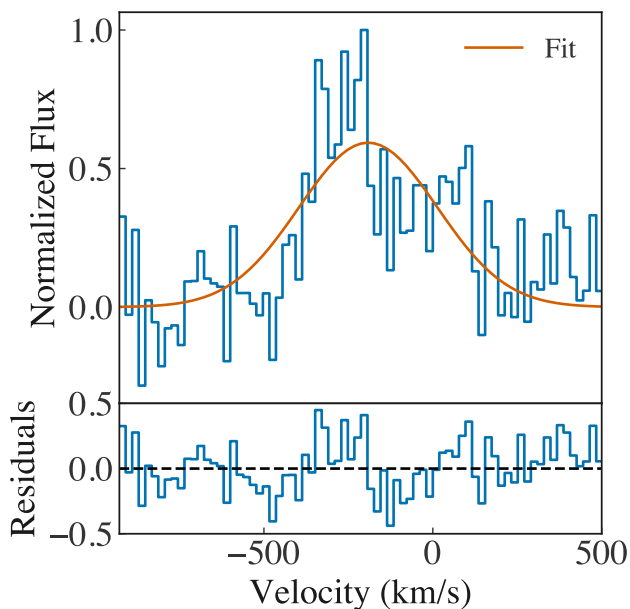


Figure 11. CO(3-2) spectrum of EGS13003805, the galaxy showing signs of asymmetry in the profile (blue curve), which cannot be corrected through the adjustment of the aperture. Overlaid is the best-fit Gaussian profile (orange line), and the bottom panel show the fit residuals.

- Cazzoli, S., Arribas, S., Maiolino, R., & Colina, L. 2016, *A&A*, 590, A125, doi: [10.1051/0004-6361/201526788](https://doi.org/10.1051/0004-6361/201526788)
- Chartas, G., Davidson, E., Brusa, M., et al. 2020, *MNRAS*, 496, 598, doi: [10.1093/mnras/staa1534](https://doi.org/10.1093/mnras/staa1534)
- Cicone, C., Feruglio, C., Maiolino, R., et al. 2012, *A&A*, 543, A99, doi: [10.1051/0004-6361/201218793](https://doi.org/10.1051/0004-6361/201218793)
- Concas, A., Maiolino, R., Curti, M., et al. 2022, *MNRAS*, 513, 2535, doi: [10.1093/mnras/stac1026](https://doi.org/10.1093/mnras/stac1026)
- Contursi, A., Poglitsch, A., Graciá Carpio, J., et al. 2013, *A&A*, 549, A118, doi: [10.1051/0004-6361/201219214](https://doi.org/10.1051/0004-6361/201219214)
- Cooper, J. L., Bicknell, G. V., Sutherland, R. S., & Bland-Hawthorn, J. 2008, *ApJ*, 674, 157, doi: [10.1086/524918](https://doi.org/10.1086/524918)
- Costa, T., Sijacki, D., & Haehnelt, M. G. 2015, *MNRAS*, 448, L30, doi: [10.1093/mnras/slu193](https://doi.org/10.1093/mnras/slu193)
- Dan, K. Y., Seebeck, J., Veilleux, S., et al. 2025, *ApJ*, 979, 68, doi: [10.3847/1538-4357/ad9a50](https://doi.org/10.3847/1538-4357/ad9a50)
- Davé, R., Finlator, K., & Oppenheimer, B. D. 2011, *MNRAS*, 416, 1354, doi: [10.1111/j.1365-2966.2011.19132.x](https://doi.org/10.1111/j.1365-2966.2011.19132.x)
- Davies, R., Shimizu, T., Pereira-Santaella, M., et al. 2024a, *A&A*, 689, A263, doi: [10.1051/0004-6361/202449875](https://doi.org/10.1051/0004-6361/202449875)

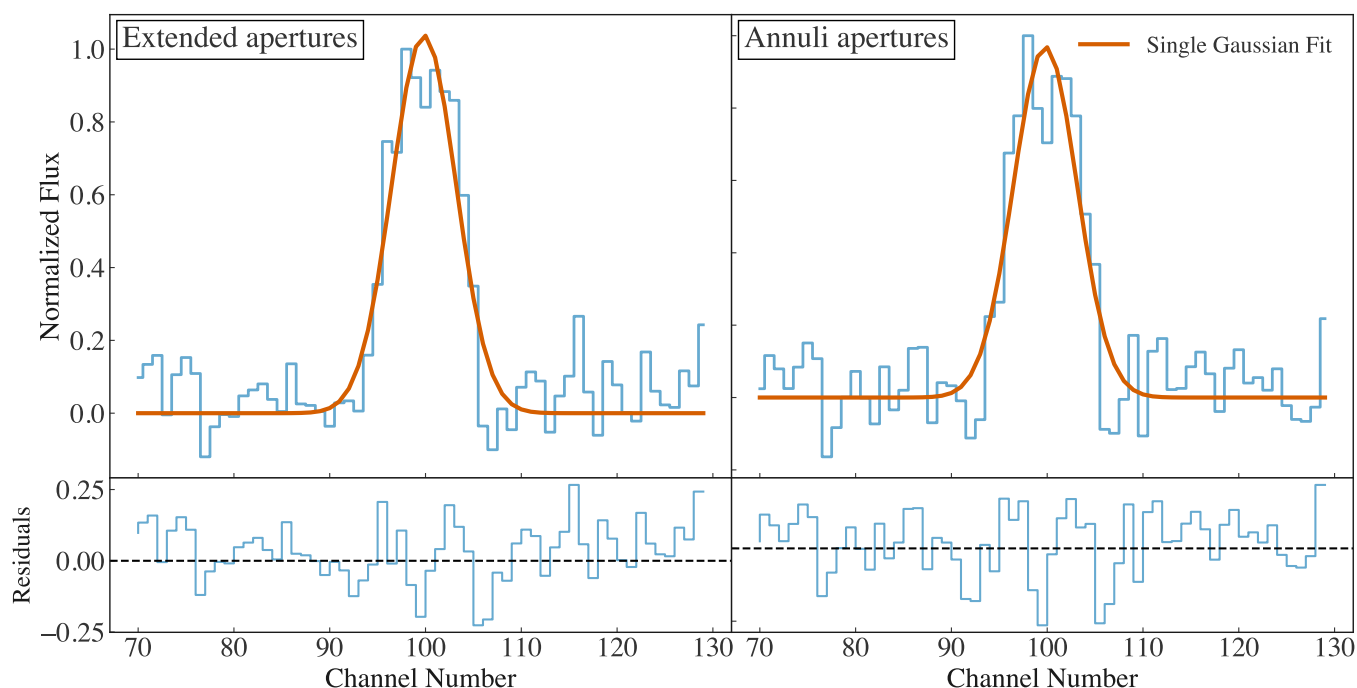


Figure 12. Stacked profiles for different apertures overlaid with the best-fit single Gaussian profile (solid red line). In both cases, fitting shows that no significant outflow component is detected in the stacked spectrum. *Left Panel:* Top: Stacked spectrum (light blue curve) of the full sample of 154 galaxies, but extracted from apertures 10kpc wider. Bottom: Residuals of the fit to the spectrum. *Right Panel:* Same as left, but extracted from apertures 10kpc wider. Bottom: Residuals of the fit to the spectrum.

Davies, R. I., Maciejewski, W., Hicks, E. K. S., et al. 2014, *ApJ*, 792, 101,

doi: [10.1088/0004-637X/792/2/101](https://doi.org/10.1088/0004-637X/792/2/101)

Davies, R. L., Förster Schreiber, N. M., Übler, H., et al. 2019, *ApJ*, 873, 122,

doi: [10.3847/1538-4357/ab06f1](https://doi.org/10.3847/1538-4357/ab06f1)

Davies, R. L., Förster Schreiber, N. M., Lutz, D., et al. 2020, *ApJ*, 894, 28,

doi: [10.3847/1538-4357/ab86ad](https://doi.org/10.3847/1538-4357/ab86ad)

Davies, R. L., Belli, S., Park, M., et al. 2024b,

MNRAS, 528, 4976, doi: [10.1093/mnras/stae327](https://doi.org/10.1093/mnras/stae327)

Dekel, A., & Silk, J. 1986, *ApJ*, 303, 39,

doi: [10.1086/164050](https://doi.org/10.1086/164050)

Delvecchio, I., Smolčić, V., Zamorani, G., et al.

2017, *A&A*, 602, A3,

doi: [10.1051/0004-6361/201629367](https://doi.org/10.1051/0004-6361/201629367)

Donley, J. L., Koekemoer, A. M., Brusa, M., et al. 2012, *ApJ*, 748, 142,

doi: [10.1088/0004-637X/748/2/142](https://doi.org/10.1088/0004-637X/748/2/142)

Erb, D. K., Quider, A. M., Henry, A. L., &

Martin, C. L. 2012, *ApJ*, 759, 26,

doi: [10.1088/0004-637X/759/1/26](https://doi.org/10.1088/0004-637X/759/1/26)

Fabian, A. C. 2012, *ARA&A*, 50, 455,

doi: [10.1146/annurev-astro-081811-125521](https://doi.org/10.1146/annurev-astro-081811-125521)

Feruglio, C., Ferrara, A., Bischetti, M., et al.

2017, *A&A*, 608, A30,

doi: [10.1051/0004-6361/201731387](https://doi.org/10.1051/0004-6361/201731387)

Fiore, F., Feruglio, C., Shankar, F., et al. 2017,

A&A, 601, A143,

doi: [10.1051/0004-6361/201629478](https://doi.org/10.1051/0004-6361/201629478)

Fluetsch, A., Maiolino, R., Carniani, S., et al.

2019, *MNRAS*, 483, 4586,

doi: [10.1093/mnras/sty3449](https://doi.org/10.1093/mnras/sty3449)

—. 2021, *MNRAS*, 505, 5753,

doi: [10.1093/mnras/stab1666](https://doi.org/10.1093/mnras/stab1666)

Förster Schreiber, N. M., & Wuyts, S. 2020,

ARA&A, 58, 661,

doi: [10.1146/annurev-astro-032620-021910](https://doi.org/10.1146/annurev-astro-032620-021910)

Förster Schreiber, N. M., Genzel, R., Newman,

S. F., et al. 2014, *ApJ*, 787, 38,

doi: [10.1088/0004-637X/787/1/38](https://doi.org/10.1088/0004-637X/787/1/38)

Förster Schreiber, N. M., Übler, H., Davies, R. L.,

et al. 2019, *ApJ*, 875, 21,

doi: [10.3847/1538-4357/ab0ca2](https://doi.org/10.3847/1538-4357/ab0ca2)

Freeman, W. R., Siana, B., Kriek, M., et al. 2019,

ApJ, 873, 102, doi: [10.3847/1538-4357/ab0655](https://doi.org/10.3847/1538-4357/ab0655)

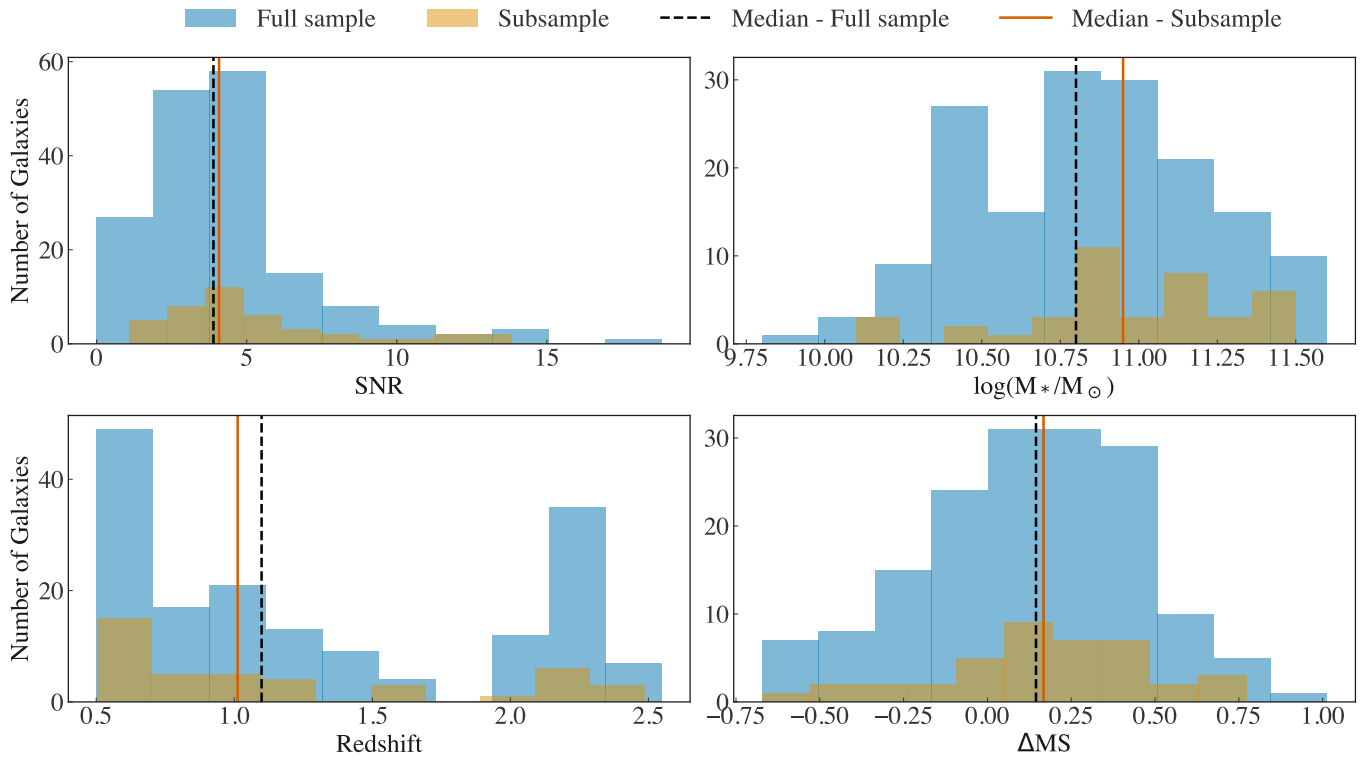


Figure 13. Comparison between properties distributions of the full sample (light blue histograms) and the subset sample (yellow histograms) showing a tentative outflow detection. The medians of each properties are also plotted for the full sample (dashed black) and the subset sample (solid orange).

- Freundlich, J., Combes, F., Tacconi, L. J., et al. 2019, *A&A*, 622, A105, doi: [10.1051/0004-6361/201732223](https://doi.org/10.1051/0004-6361/201732223)
- Genzel, R., Newman, S., Jones, T., et al. 2011, *ApJ*, 733, 101, doi: [10.1088/0004-637X/733/2/101](https://doi.org/10.1088/0004-637X/733/2/101)
- Genzel, R., Förster Schreiber, N. M., Rosario, D., et al. 2014, *ApJ*, 796, 7, doi: [10.1088/0004-637X/796/1/7](https://doi.org/10.1088/0004-637X/796/1/7)
- González-Alfonso, E., Fischer, J., Spoon, H. W. W., et al. 2017, *ApJ*, 836, 11, doi: [10.3847/1538-4357/836/1/11](https://doi.org/10.3847/1538-4357/836/1/11)
- Harrison, C. M., & Ramos Almeida, C. 2024, *Galaxies*, 12, 17, doi: [10.3390/galaxies12020017](https://doi.org/10.3390/galaxies12020017)
- Harrison, C. M., Alexander, D. M., Mullaney, J. R., et al. 2016, *MNRAS*, 456, 1195, doi: [10.1093/mnras/stv2727](https://doi.org/10.1093/mnras/stv2727)
- Herrera-Camus, R., Tacconi, L., Genzel, R., et al. 2019, *ApJ*, 871, 37, doi: [10.3847/1538-4357/aaf6a7](https://doi.org/10.3847/1538-4357/aaf6a7)
- Herrera-Camus, R., Janssen, A., Sturm, E., et al. 2020a, *A&A*, 635, A47, doi: [10.1051/0004-6361/201936434](https://doi.org/10.1051/0004-6361/201936434)
- Herrera-Camus, R., Sturm, E., Graciá-Carpio, J., et al. 2020b, *A&A*, 633, L4, doi: [10.1051/0004-6361/201937109](https://doi.org/10.1051/0004-6361/201937109)
- Herrera-Camus, R., Janssen, A., Sturm, E., et al. 2020c, *A&A*, 635, A47, doi: [10.1051/0004-6361/201936434](https://doi.org/10.1051/0004-6361/201936434)
- Hogg, D. W., Bovy, J., & Lang, D. 2010, arXiv e-prints, arXiv:1008.4686, doi: [10.48550/arXiv.1008.4686](https://doi.org/10.48550/arXiv.1008.4686)
- Hopkins, P. F., Kereš, D., Oñorbe, J., et al. 2014, *MNRAS*, 445, 581, doi: [10.1093/mnras/stu1738](https://doi.org/10.1093/mnras/stu1738)
- Jolly, J.-B., Knudsen, K. K., & Stanley, F. 2020, *MNRAS*, 499, 3992, doi: [10.1093/mnras/staa2908](https://doi.org/10.1093/mnras/staa2908)
- Kehoe, E., Shapley, A. E., Schreiber, N. M. F., et al. 2024, *ApJ*, 976, 28, doi: [10.3847/1538-4357/ad7ebb](https://doi.org/10.3847/1538-4357/ad7ebb)
- Kewley, L. J., Maier, C., Yabe, K., et al. 2013, *ApJL*, 774, L10, doi: [10.1088/2041-8205/774/1/L10](https://doi.org/10.1088/2041-8205/774/1/L10)
- King, A., & Pounds, K. 2015, *ARA&A*, 53, 115, doi: [10.1146/annurev-astro-082214-122316](https://doi.org/10.1146/annurev-astro-082214-122316)
- Krieger, N., Bolatto, A. D., Walter, F., et al. 2019, *ApJ*, 881, 43, doi: [10.3847/1538-4357/ab2d9c](https://doi.org/10.3847/1538-4357/ab2d9c)
- Kriek, M., Shapley, A. E., Reddy, N. A., et al. 2015, *ApJS*, 218, 15, doi: [10.1088/0067-0049/218/2/15](https://doi.org/10.1088/0067-0049/218/2/15)
- Leroy, A. K., Walter, F., Martini, P., et al. 2015, *ApJ*, 814, 83, doi: [10.1088/0004-637X/814/2/83](https://doi.org/10.1088/0004-637X/814/2/83)
- Leung, G. C. K., Coil, A. L., Azadi, M., et al. 2017, *ApJ*, 849, 48, doi: [10.3847/1538-4357/aa9024](https://doi.org/10.3847/1538-4357/aa9024)
- Leung, G. C. K., Coil, A. L., Aird, J., et al. 2019, *ApJ*, 886, 11, doi: [10.3847/1538-4357/ab4a7c](https://doi.org/10.3847/1538-4357/ab4a7c)
- Levy, R. C., Bolatto, A. D., Leroy, A. K., et al. 2021, *ApJ*, 912, 4, doi: [10.3847/1538-4357/abec84](https://doi.org/10.3847/1538-4357/abec84)
- Liddle, A. R. 2007, *MNRAS*, 377, L74, doi: [10.1111/j.1745-3933.2007.00306.x](https://doi.org/10.1111/j.1745-3933.2007.00306.x)
- Lutz, D., Sturm, E., Janssen, A., et al. 2020, *A&A*, 633, A134, doi: [10.1051/0004-6361/201936803](https://doi.org/10.1051/0004-6361/201936803)
- Madau, P., & Dickinson, M. 2014, *ARA&A*, 52, 415, doi: [10.1146/annurev-astro-081811-125615](https://doi.org/10.1146/annurev-astro-081811-125615)
- Murray, N., Quataert, E., & Thompson, T. A. 2005, *ApJ*, 618, 569, doi: [10.1086/426067](https://doi.org/10.1086/426067)
- Mutch, S. J., Croton, D. J., & Poole, G. B. 2013, *MNRAS*, 435, 2445, doi: [10.1093/mnras/stt1453](https://doi.org/10.1093/mnras/stt1453)
- Newman, S. F., Genzel, R., Förster-Schreiber, N. M., et al. 2012a, *ApJ*, 761, 43, doi: [10.1088/0004-637X/761/1/43](https://doi.org/10.1088/0004-637X/761/1/43)
- Newman, S. F., Shapiro Griffin, K., Genzel, R., et al. 2012b, *ApJ*, 752, 111, doi: [10.1088/0004-637X/752/2/111](https://doi.org/10.1088/0004-637X/752/2/111)
- Parlanti, E., Carniani, S., Venturi, G., et al. 2024, arXiv e-prints, arXiv:2407.19008, doi: [10.48550/arXiv.2407.19008](https://doi.org/10.48550/arXiv.2407.19008)
- Peebles, M. S., Werk, J. K., Tumlinson, J., et al. 2014, *ApJ*, 786, 54, doi: [10.1088/0004-637X/786/1/54](https://doi.org/10.1088/0004-637X/786/1/54)
- Péroux, C., & Howk, J. C. 2020, *ARA&A*, 58, 363, doi: [10.1146/annurev-astro-021820-120014](https://doi.org/10.1146/annurev-astro-021820-120014)
- Ramos Almeida, C., Acosta-Pulido, J. A., Tadhunter, C. N., et al. 2019, *MNRAS*, 487, L18, doi: [10.1093/mnras/slz072](https://doi.org/10.1093/mnras/slz072)
- Ramos Almeida, C., Bischetti, M., García-Burillo, S., et al. 2022, *A&A*, 658, A155, doi: [10.1051/0004-6361/202141906](https://doi.org/10.1051/0004-6361/202141906)
- Reddy, N. A., Kriek, M., Shapley, A. E., et al. 2015, *ApJ*, 806, 259, doi: [10.1088/0004-637X/806/2/259](https://doi.org/10.1088/0004-637X/806/2/259)
- Reichardt Chu, B., Fisher, D. B., Bolatto, A. D., et al. 2022, *ApJ*, 941, 163, doi: [10.3847/1538-4357/aca1bd](https://doi.org/10.3847/1538-4357/aca1bd)
- Reichardt Chu, B., Fisher, D. B., Chisholm, J., et al. 2025, *MNRAS*, 536, 1799, doi: [10.1093/mnras/stae2705](https://doi.org/10.1093/mnras/stae2705)

- Richings, A. J., & Faucher-Giguère, C.-A. 2018, *MNRAS*, 478, 3100, doi: [10.1093/mnras/sty1285](https://doi.org/10.1093/mnras/sty1285)
- Riffel, R. A., Storchi-Bergmann, T., Riffel, R., et al. 2023, *MNRAS*, 521, 1832, doi: [10.1093/mnras/stad599](https://doi.org/10.1093/mnras/stad599)
- Roberts-Borsani, G. W., & Saintonge, A. 2019, *MNRAS*, 482, 4111, doi: [10.1093/mnras/sty2824](https://doi.org/10.1093/mnras/sty2824)
- Rodighiero, G., Daddi, E., Baronchelli, I., et al. 2011, *ApJL*, 739, L40, doi: [10.1088/2041-8205/739/2/L40](https://doi.org/10.1088/2041-8205/739/2/L40)
- Rubin, K. H. R., Prochaska, J. X., Koo, D. C., et al. 2014, *ApJ*, 794, 156, doi: [10.1088/0004-637X/794/2/156](https://doi.org/10.1088/0004-637X/794/2/156)
- Rupke, D. S., Veilleux, S., & Sanders, D. B. 2005, *ApJS*, 160, 115, doi: [10.1086/432889](https://doi.org/10.1086/432889)
- Rupke, D. S. N. 2018, *Galaxies*, 6, 138, doi: [10.3390/galaxies6040138](https://doi.org/10.3390/galaxies6040138)
- Sanders, R. L., Shapley, A. E., Kriek, M., et al. 2018, *ApJ*, 858, 99, doi: [10.3847/1538-4357/aabcbdb](https://doi.org/10.3847/1538-4357/aabcbdb)
- Schaye, J., Crain, R. A., Bower, R. G., et al. 2015, *MNRAS*, 446, 521, doi: [10.1093/mnras/stu2058](https://doi.org/10.1093/mnras/stu2058)
- Schneider, E. E., Ostriker, E. C., Robertson, B. E., & Thompson, T. A. 2020, *ApJ*, 895, 43, doi: [10.3847/1538-4357/ab8ae8](https://doi.org/10.3847/1538-4357/ab8ae8)
- Schneider, E. E., Robertson, B. E., & Thompson, T. A. 2018, *ApJ*, 862, 56, doi: [10.3847/1538-4357/aacce1](https://doi.org/10.3847/1538-4357/aacce1)
- Schwarz, G. 1978, *Annals of Statistics*, 6, 461
- Shapley, A. E., Steidel, C. C., Pettini, M., & Adelberger, K. L. 2003, *ApJ*, 588, 65, doi: [10.1086/373922](https://doi.org/10.1086/373922)
- Shapley, A. E., Reddy, N. A., Kriek, M., et al. 2015, *ApJ*, 801, 88, doi: [10.1088/0004-637X/801/2/88](https://doi.org/10.1088/0004-637X/801/2/88)
- Solomon, P. M., Downes, D., Radford, S. J. E., & Barrett, J. W. 1997, *ApJ*, 478, 144, doi: [10.1086/303765](https://doi.org/10.1086/303765)
- Speagle, J. S., Steinhardt, C. L., Capak, P. L., & Silverman, J. D. 2014, *ApJS*, 214, 15, doi: [10.1088/0067-0049/214/2/15](https://doi.org/10.1088/0067-0049/214/2/15)
- Stanley, F., Jolly, J. B., König, S., & Knudsen, K. K. 2019, *A&A*, 631, A78, doi: [10.1051/0004-6361/201834530](https://doi.org/10.1051/0004-6361/201834530)
- Steidel, C. C., Erb, D. K., Shapley, A. E., et al. 2010, *ApJ*, 717, 289, doi: [10.1088/0004-637X/717/1/289](https://doi.org/10.1088/0004-637X/717/1/289)
- Sturm, E., González-Alfonso, E., Veilleux, S., et al. 2011, *ApJL*, 733, L16, doi: [10.1088/2041-8205/733/1/L16](https://doi.org/10.1088/2041-8205/733/1/L16)
- Sugahara, Y., Ouchi, M., Lin, L., et al. 2017, *ApJ*, 850, 51, doi: [10.3847/1538-4357/aa956d](https://doi.org/10.3847/1538-4357/aa956d)
- Swinbank, A. M., Harrison, C. M., Tiley, A. L., et al. 2019, *MNRAS*, 487, 381, doi: [10.1093/mnras/stz1275](https://doi.org/10.1093/mnras/stz1275)
- Symeonidis, M., Georgakakis, A., Page, M. J., et al. 2014, *MNRAS*, 443, 3728, doi: [10.1093/mnras/stu1441](https://doi.org/10.1093/mnras/stu1441)
- Tacconi, L. J., Genzel, R., & Sternberg, A. 2020, *ARA&A*, 58, 157, doi: [10.1146/annurev-astro-082812-141034](https://doi.org/10.1146/annurev-astro-082812-141034)
- Tacconi, L. J., Neri, R., Genzel, R., et al. 2013, *ApJ*, 768, 74, doi: [10.1088/0004-637X/768/1/74](https://doi.org/10.1088/0004-637X/768/1/74)
- Tacconi, L. J., Genzel, R., Saintonge, A., et al. 2018, *ApJ*, 853, 179, doi: [10.3847/1538-4357/aaa4b4](https://doi.org/10.3847/1538-4357/aaa4b4)
- Talia, M., Mignoli, M., Cimatti, A., et al. 2012, *A&A*, 539, A61, doi: [10.1051/0004-6361/201117683](https://doi.org/10.1051/0004-6361/201117683)
- Talia, M., Brusa, M., Cimatti, A., et al. 2017, *MNRAS*, 471, 4527, doi: [10.1093/mnras/stx1788](https://doi.org/10.1093/mnras/stx1788)
- Taylor, E., Maltby, D., Almaini, O., et al. 2024, *MNRAS*, 535, 1684, doi: [10.1093/mnras/stae2463](https://doi.org/10.1093/mnras/stae2463)
- Tozzi, G., Cresci, G., Marasco, A., et al. 2021, *A&A*, 648, A99, doi: [10.1051/0004-6361/202040190](https://doi.org/10.1051/0004-6361/202040190)
- Tumlinson, J., Peebles, M. S., & Werk, J. K. 2017, *ARA&A*, 55, 389, doi: [10.1146/annurev-astro-091916-055240](https://doi.org/10.1146/annurev-astro-091916-055240)
- Vayner, A., Zakamska, N., Wright, S. A., et al. 2021, *ApJ*, 923, 59, doi: [10.3847/1538-4357/ac2b9e](https://doi.org/10.3847/1538-4357/ac2b9e)
- Veilleux, S., Bolatto, A., Tombesi, F., et al. 2017, *ApJ*, 843, 18, doi: [10.3847/1538-4357/aa767d](https://doi.org/10.3847/1538-4357/aa767d)
- Veilleux, S., Cecil, G., & Bland-Hawthorn, J. 2005, *ARA&A*, 43, 769, doi: [10.1146/annurev.astro.43.072103.150610](https://doi.org/10.1146/annurev.astro.43.072103.150610)
- Veilleux, S., Maiolino, R., Bolatto, A. D., & Aalto, S. 2020, *A&A Rv*, 28, 2, doi: [10.1007/s00159-019-0121-9](https://doi.org/10.1007/s00159-019-0121-9)
- Veilleux, S., Meléndez, M., Sturm, E., et al. 2013, *ApJ*, 776, 27, doi: [10.1088/0004-637X/776/1/27](https://doi.org/10.1088/0004-637X/776/1/27)
- Vijayan, A., & Krumholz, M. R. 2024, *MNRAS*, 532, 4132, doi: [10.1093/mnras/stae1679](https://doi.org/10.1093/mnras/stae1679)
- Vijayan, A., Krumholz, M. R., & Wibking, B. D. 2024, *MNRAS*, 527, 10095, doi: [10.1093/mnras/stad3816](https://doi.org/10.1093/mnras/stad3816)
- Walter, F., Weiss, A., & Scoville, N. 2002, *ApJL*, 580, L21, doi: [10.1086/345287](https://doi.org/10.1086/345287)

- Ward, S. R., Costa, T., Harrison, C. M., & Mainieri, V. 2024, MNRAS, 533, 1733, doi: [10.1093/mnras/stae1816](https://doi.org/10.1093/mnras/stae1816)
- Weldon, A., Reddy, N. A., Topping, M. W., et al. 2022, MNRAS, 515, 841, doi: [10.1093/mnras/stac1822](https://doi.org/10.1093/mnras/stac1822)
- Weldon, A., Reddy, N. A., Coil, A. L., et al. 2024, MNRAS, 531, 4560, doi: [10.1093/mnras/stae1428](https://doi.org/10.1093/mnras/stae1428)
- Whitaker, K. E., Franx, M., Leja, J., et al. 2014, ApJ, 795, 104, doi: [10.1088/0004-637X/795/2/104](https://doi.org/10.1088/0004-637X/795/2/104)
- Zhu, G. B., Comparat, J., Kneib, J.-P., et al. 2015, ApJ, 815, 48, doi: [10.1088/0004-637X/815/1/48](https://doi.org/10.1088/0004-637X/815/1/48)